

# Composition Design of Shape Memory Ceramics based on Gaussian Processes

Ashutosh Pandey<sup>a</sup>, Justin Jetter<sup>b</sup>, Hanlin Gu<sup>c</sup>, Eckhard Quandt<sup>b</sup>, and Richard D. James<sup>\*a</sup>

<sup>a</sup>Department of Aerospace Engineering and Mechanics, University of Minnesota, Minneapolis, MN, USA

<sup>b</sup>Institute for Materials Science, Faculty of Engineering, Kiel University, Kiel, Germany

<sup>c</sup>Department of Mechanics and Engineering Science, Peking University, Beijing, China

## Abstract

We present a Gaussian process machine learning model to accurately predict the transformation temperature and lattice parameters of ZrO<sub>2</sub>-based ceramics doped with HfO<sub>2</sub>, YTaO<sub>4</sub>, and Er<sub>2</sub>O<sub>3</sub>. Our overall goal is to search for a shape memory ceramic material with a reversible transformation and low hysteresis. The input space of the model consists of key physical features derived from the electronic and bonding properties of the cations present in the compositions. The identification of a new low hysteresis composition is based on design criteria that have been successful in metal alloys: (1)  $\lambda_2 = 1$ , where  $\lambda_2$  is the middle eigenvalue of the transformation stretch tensor [1, 2, 3], (2) minimizing the  $\max|q(f)|$ , which measures the deviation from satisfying the cofactor conditions [4, 5, 6], (3) high transformation temperature, (4) low transformational volume change, and (5) solid solubility. To identify a new composition satisfying the design criteria, we develop an algorithm to generate many synthetic compositions within the mole fraction ranges of the compositional space used to generate the training data for the model. Using the predicted lattice parameters of the synthetic compositions, a strong correlation between  $\lambda_2$  and  $\max|q(f)|$  is found. We identify a promising composition, 31.75Zr-37.75Hf-14.5Y-14.5Ta-1.5Er, which closely satisfies all the design criteria. However, differential thermal analysis reveals a relatively high thermal hysteresis of 137°C for this composition, indicating that the proposed design criteria are not universally applicable to all ZrO<sub>2</sub>-based ceramics. We also explore reducing tetragonality of the austenite phase by addition of Er<sub>2</sub>O<sub>3</sub>. The idea is to tune the lattice parameters of austenite phase towards a cubic structure will increase the number of martensite variants, thus, allowing more flexibility for them to accommodate high strain during transformation compared to tetragonal to monoclinic transformation. We find the effect of Er<sub>2</sub>O<sub>3</sub> on tetragonality is weak due to limited solubility. We conclude that a more effective dopant is needed to achieve significant tetragonality reduction. Overall, Gaussian process machine learning models are shown to be highly useful for prediction of compositions and lattice parameters, but the discovery of low hysteresis ceramic materials apparently involves other factors not relevant to phase transformations in metals.

---

\*Corresponding author: james@umn.edu

# Contents

<b>1</b>	<b>Introduction</b>	<b>2</b>
<b>2</b>	<b>Prediction of transformation temperature</b>	<b>4</b>
2.1	Search for correlated physical features . . . . .	5
2.2	Machine learning models for transformation temperature . . . . .	6
<b>3</b>	<b>Prediction of lattice parameters</b>	<b>9</b>
3.1	Predictions of monoclinic crystal’s lattice parameters . . . . .	10
3.2	Predictions of tetragonal crystal’s lattice parameters . . . . .	11
<b>4</b>	<b>Theory of reversibility of phase transformation</b>	<b>12</b>
4.1	Cofactor conditions . . . . .	14
4.2	Multiple transformation correspondences . . . . .	16
4.3	Identification of shape memory ceramics with low hysteresis . . . . .	19
<b>5</b>	<b>Analysis of compositions</b>	<b>20</b>
5.1	Synthetic compositions and prediction of its properties . . . . .	20
5.2	Selection of synthetic composition for experiment . . . . .	21
5.3	Experimental Methodology & results . . . . .	22
<b>6</b>	<b>Conclusion</b>	<b>24</b>

## 1 Introduction

The shape memory effect is based on a thermally induced, reversible phase transformation between a high-temperature austenite phase and a low-temperature martensite phase. During a forward transformation, the austenite phase is cooled down to a certain temperature  $M_s$ , when the martensite first appears. With further cooling, the austenite phase completely transforms into the martensite at the martensite finish temperature  $M_f$ . The reverse transformation upon heating causes transformation back to the austenite, as indicated by the austenite start  $A_s$  and finish  $A_f$  temperatures. The austenite phase has higher symmetry than the martensite phase, leading to symmetry-related variants of martensite [7]. Due to compatibility with the austenite phase, the martensite phase typically appears as finely twinned laminates [8, 9, 10] on cooling consisting of two variants of martensite with volume fractions  $f$  and  $(1 - f)$ .

Generally, a stressed transition layer separates the twinned martensite and austenite, leading to average compatibility between phases. The reversibility of the phase transformation, measured by the width of the hysteresis loop [3, 11] or by the number of cycles to failure [12, 13], can be achieved by improving the compatibility of the two phases. Generally, there is an equipartition between the elastic energy of the stressed transition layer and the total interfacial energy of the twin boundaries [14, 15]. The process of tuning geometric compatibility entails devising strategies to reduce elastic energy in the transition layer by adjusting lattice parameters via compositional changes [16]. This is thought to improve the reversibility of the transformation by two distinct mechanisms: 1) It removes an energy barrier associated to the creation of these stressed transition layers during transformation [2] and 2) it mitigates against plastic deformation in these stressed layers as they move through the material during transformation.

Necessary and sufficient conditions for eliminating this transition layer in a simple austenite/martensite interface is the condition  $\lambda_2 = 1$ , explained below. Under stronger conditions ( $\lambda_2 = 1$  plus additional conditions), stressed transition layers are not only eliminated for simple austenite/twinned martensite interfaces, but also in a wide variety of complex microstructures involving multiple austenite/martensite interfaces relevant to nucleation and growth. These stronger conditions are termed conditions of supercompatibility. Within the theory of martensite [17, 18] the *cofactor conditions*, introduced in the [4, 5] are notable conditions of supercompatibility. Like  $\lambda_2 = 1$  they are purely geometrical; they only involve the lattice parameters of the two phases. The strategy of tuning lattice parameters by compositional changes has been used successfully in metals to lower thermal hysteresis to a few degrees K [3, 19, 20] or to increase the fatigue life under repeated stress-induced transformation (in tension) [12] to  $10^7$  cycles.

Discovering a ceramic material with a phase transformation that could exhibit a reversible shape memory effect could enable diverse applications in aerospace engineering, biomedicine and energy science. This discovery could serve as a basis for a reversible, low-hysteresis actuator that could function in high temperature or corrosive environments. Since ceramics can exhibit ferroelectricity, this could potentially extend the set of known ferroelectrics, with interesting applications to energy conversion in the small temperature difference regime [21]. Among ceramics, ZrO<sub>2</sub>-based ceramics are of special technological interest because the martensitic phase transformation in these materials is accompanied by a transformation strain of up to 10% in shear and up to 3-5% in volume. They undergo phase transformation from the austenite with a tetragonal crystal structure to the martensite with a monoclinic crystal structure. The achievable actuation stress in these ceramics is around  $2 \times 10^3$  MPa [22], offering high work output approaching 100 MJ/m<sup>3</sup>, thus making it ideal for solid state actuator.

Recently, there have been efforts in applying the cofactor conditions to Zirconia-based ceramics [6, 23, 24, 25] to search for a low thermal hysteresis shape memory ceramic (SMC). The thermal hysteresis ( $\Delta T$ ) is determined as half the difference between the ( $A_s + A_f$ ) and the ( $M_s + M_f$ ). For example, Gu et al. [6] discovered the lowest hysteresis in ceramic (Zr<sub>0.45</sub>Hf<sub>0.55</sub>O<sub>2</sub>)<sub>0.775</sub> - (Y<sub>0.5</sub>Nb<sub>0.5</sub>O<sub>2</sub>)<sub>0.225</sub> with thermal hysteresis  $\Delta T = 134$  °C by employing new criteria based on minimizing the maximum deviation from the exact satisfaction of the cofactor condition; while Pang et al. [25] proposed design criteria to guide the discovery of ceramics with low hysteresis, which are "(1) commensurate interfaces between transforming phases (close satisfaction of cofactor condition) (2) low transformation volume change (3) solid solubility (4) high transformation temperature (martensite start temperature > 773 K)". They looked at how adding different dopants to Zirconia affected the design criteria and found a group of dopants that when added to Zirconia would likely meet the design criteria. They discovered that Zirconia doped with 17Ti-3Al-6Cr, and with 20Ti-5Al has hysteresis values of 29 K and 15 K, respectively<sup>1</sup>

Some of the conditions in the design criteria proposed in the previous studies for discovering low hysteresis SMC need further investigation. For example, in Gu et al.'s work [6], searching for a low hysteresis SMC is based on minimizing the maximum deviation ( $\max|q(f)|$ ) from the exact satisfaction of the cofactor condition. The maximum deviation would exist at a particular configuration of the twinned structure of martensite with austenite for any composition. Let's suppose that the maximum deviation exists when the volume fraction of one of the variants in

<sup>1</sup>They measured hysteresis using Diffraction Scanning Calorimetry (DSC), and by our method using Differential Thermal Analysis (DTA), the hysteresis values in these samples are found to be around 135 K and 116 K, respectively.

the twinned martensite is  $f_1$ . If the maximum deviation always exists near some particular value of  $f_1$ , irrespective of the chosen composition, then the  $q(f)$  expression could be further simplified based on values of  $f_1$ .

Similarly, the design criteria proposed by Pang et al. [25] are applied to compositions having new dopants to check its universality to search for low hysteresis ceramics. One possible dopant candidate is Erbium oxide ( $\text{Er}_2\text{O}_3$ ), which, when added to Zirconia, is known to reduce the tetragonality [26] of the austenite phase. Reducing the tetragonality of the austenite phase towards a cubic crystal structure offers more degrees of freedom during transformation. This is because the phase transformation from the cubic to the monoclinic crystal structure has 24 variants of martensite, compared to only having 12 variants of martensite for the phase transformation from the tetragonal to monoclinic. The availability of more variants in the cubic to monoclinic phase transformation makes this transformation more flexible, allowing them to accommodate high strain during transformation. Therefore, reducing the tetragonality of the austenite phase might lead to a low hysteresis SMC. We fabricate compositions in which Zirconia is doped with Erbium oxide, and search for a sample in the compositional space that satisfies the design criteria proposed by Pang, to search for a low hysteresis sample.

The objective of this research is to investigate the design criteria presented in the literature to find the conditions that strongly affect thermal hysteresis in ceramics. To conduct this study, we first explore a data-driven methodology that involves identifying physical features based on electronic and crystal structure parameters that strongly correlate with transformation temperature and lattice parameters. We focus here on developing a predictive data-driven capability based on the Gaussian processes (GP) to predict transformation temperatures and lattice parameters of new compositions using physical features as input data. In order to generate new compositions, an algorithm has been developed to generate a wide range of synthetic compositions within the composition space of experimental mole fractions of oxides in ceramic. The predicted lattice parameters of all synthetic compositions are used to calculate the maximum deviation from the exact satisfaction of the cofactor condition. This process generates data to observe a strong correlation between the maximum deviation and  $\lambda_2$ , suggesting that most of the maximum deviation values are found at the  $f_1 = 0$  or at  $f_1 = 1$ .

Our strategy identifies a composition "31.75Zr-37.75Hf-14.5Y-14.5Ta-1.5Er" whose predicted transformation temperature and lattice parameters are validated by our experimental work with high accuracy. Therefore, this strategy can be generalized to other multi-component ceramic systems to optimize their properties. The composition 31.75Zr-37.75Hf-14.5Y-14.5Ta-1.5Er satisfies the design criteria proposed by Pang et al. [25]. However, it still has a significant thermal hysteresis of 137 °C during the differential thermal analysis (DTA) experiment. This establishes that the criteria proposed by Pang et al. are not universal for every ceramic system.

## 2 Prediction of transformation temperature

Transformation temperature is the temperature such that the change in total free energy between the austenite and the martensite phases of a system is zero, and the system is said to be in thermoelastic equilibrium. The start and finish temperatures for forward transformation  $M_s$  and  $M_f$ , and the temperatures for reverse transformation  $A_s$  and  $A_f$  plays an important role in finding the range of temperatures at which thermoelastic equilibrium occurs. Tang and Wayman [27] found the range of thermoelastic equilibrium to be confined between  $T_o$  and  $T'_o$ , where  $T_o = \frac{1}{2}(M_s + A_f)$  and  $T'_o = \frac{1}{2}(M_f + A_s)$ . Thus, for any temperature  $T$  between

$T_o$  and  $T'_o$  ( $T_o > T > T'_o$ ), the thermoelastic equilibrium can be obtained. In this work, we have approximated the transformation temperature  $T_f$  as the average of the four characteristic temperatures, i.e.,  $\frac{1}{4}(M_s + M_f + A_s + A_f)$  [2].

In this section, we discuss the set of dopants that are added to  $ZrO_2$  to synthesize ceramic compositions. These compositions are used to derive the set of key physical features based on electronic and crystal structure properties. The features are used as input to a machine learning (ML) model that predicts  $T_f$ . The ML model capable of predicting  $T_f$  plays a key role in searching for ceramic composition with targeted  $T_f$ . This model will be referred to as  $ML_T$ . We compare key non-parametric ML methods for the model and choose the best-performing method for the  $ML_T$ . Furthermore, the lattice parameters of the monoclinic and tetragonal crystal structure usually exhibit a significant correlation with  $T_f$ . Therefore, the predicted  $T_f$  by the  $ML_T$  may serve as an input parameter for the subsequent construction of another ML model for predicting lattice parameters.

Among many possible dopants, we add selected dopants to  $ZrO_2$  such that a ceramic system with high  $M_s$  is discovered to satisfy one of the design criteria of Pang et al., i.e., high transformation temperature ( $M_s > 500$  °C) [25]. Also, as discussed in the introduction, the dopants should reduce the tetragonality of the composition's austenite phase. It is well known that alloying  $HfO_2$  into  $ZrO_2$  sharply increases the  $A_s$  and  $M_s$  temperatures [25][28]. Additionally, the alloying of  $HfO_2$  in Ytria-stabilized Zirconia slightly increases the tetragonality of the austenite phase [28]; however, it is still added in the ceramic system as it significantly elevates the  $T_f$  of the composition compared to other oxides [25]. The dopants that reduces the tetragonality of the austenite phase are  $Er_2O_3$  and mixture of Ytria and Tantalum pentoxide in a 1:1 ratio i.e.,  $Y_{0.5}Ta_{0.5}O_2$  [29][28]. Lower mole fraction ( $m$ ) values of  $Er_2O_3$   $\{m_{Er_2O_3} | 0.01 \leq m_{Er_2O_3} \leq 0.03\}$  sharply decreases the tetragonality as compared to the same amount of  $Y_{0.5}Ta_{0.5}O_2$  in  $ZrO_2$ . Although, both  $Er_2O_3$  and  $Y_{0.5}Ta_{0.5}O_2$  reduces the  $T_f$  of the doped  $ZrO_2$  based composition, however, limiting the  $m_{Y_{0.5}Ta_{0.5}O_2}$  upto 0.18 keeps the  $T_f$  well above 500 °C [30]. Similarly, limiting the  $m_{Er_2O_3} \leq 0.03$  in  $ZrO_2$  keeps the  $T_f$  well above 500 °C [31]. Hence, we represent the ceramic system as  $(ZrO_2)_{m_1} - (HfO_2)_{m_2} - (Er_2O_3)_{m_3} - (Y_{0.5}Ta_{0.5}O_2)_{m_4}$ , where  $m_4 = 1 - (m_1 + m_2 + m_3)$ . We synthesize 44 compositions in which the mole fraction  $m_j$  of each oxide are constrained as  $0.1675 \leq m_1 \leq 0.71$ ,  $0.1675 \leq m_2 \leq 0.5677$ ,  $0.0 \leq m_3 \leq 0.055$  and  $0.025 \leq m_4 \leq 0.175$ . During the synthesis process, the same processing conditions are applied to all 44 compositions to mitigate any effect of processing and microstructural changes.

In the next subsection, we discuss the set of key physical features and a way to derive average value of the physical features for a given ceramic system.

## 2.1 Search for correlated physical features

We discuss here the importance of selecting the relevant features that form the input to the ML models. Recently, there have been efforts in literature to understand a strong correlation between the  $T_f$  and the physical features derived from the composition of the ceramic system. For example, Zarinejad et al. [32] doped  $ZrO_2$  with different oxides such as  $HfO_2$ ,  $Y_2O_3$ ,  $CeO_2$ ,  $MgO$ ,  $CaO$  and  $TiO_2$  and depending on the chemical composition, found a clear correlation of the  $T_f$  with the number of valence electrons ( $ev$ ), valence electron ratio ( $VER$ ), and the atomic number ( $Z$ ). They found that the  $A_s$  and  $M_s$  temperatures decrease with the increase in the  $VER$  and the  $ev$ . However, a general trend of increasing the  $T_f$  with average  $Z$  of the

ceramic is observed. Similarly, Frenzel et al. [33] found a strong compositional dependence of  $M_s$  in binary Ni-Ti, ternary Ni-Ti-Cr, and Ni-Ti-Cu alloys based on a strong stabilization of B2 austenite (resembling cubic cesium chloride type structure) through the formation of antisite defects. Thus, we also assume a likelihood of the formation of antisite defects influencing  $T_f$  in ceramic oxides. Key factors causing antisite defects include stoichiometry, atomic size mismatch, and electronegativity.

Following the literature, we consider the following physical features that might strongly affect the  $T_f$  in SMC: atomic number ( $Z$ ), Clementi’s atomic radius ( $r_{cle}$ ), Pettifor chemical scale ( $cs$ ), Pauling electronegativity ( $en$ ), electron affinity ( $eff$ ), valence electrons ( $ev$ ), Shannon ionic radius ( $rio$ ), and Slater atomic radius ( $rsla$ ). The average value of the physical features,  $x$ , for the composition  $(ZrO_2)_{m_1}-(HfO_2)_{m_2}-(Er_2O_3)_{m_3}-(Y_{0.5}Ta_{0.5}O_2)_{m_4}$ , are based upon a linear combination of weighted feature values of the cations in the composition. We use the mole fraction value  $m_k$  of each oxide  $k$  as the weight and represent  $x$  in Eq. 1 as:

$$x = \sum_{k=1}^{n_c} m_k p_k \quad (1)$$

The value of a physical feature for the cation of the oxide  $k$  is represented by  $p_k$ . The total no. of cations considered for creating the ceramic system is represented by  $n_c$ .

We also define the valence electron ratio ( $VER$ ) to be one of the physical features in our study.  $VER$  is defined as the ratio of the average number of valence electrons to the average atomic number of the composition, defined as:

$$VER = \frac{\sum_{k=1}^{n_c} m_k (ev)_k}{\sum_{k=1}^{n_c} m_k Z_k} \quad (2)$$

Where  $Z_k$  is the atomic number of cation that belongs to oxide  $k$ . The set of physical features  $\mathbf{x}$  derived from a ceramic system using Eq. 1 and Eq. 2 are listed in Table 1. Some of these features might strongly correlate with each other, leading to the use of redundant information as input to the ML model. To identify the redundant features, we visualize the correlation among all features on Pearson correlation map [34] in Fig. 1, where a full blue circle indicates a +1 value of correlation. In comparison, a full red circle indicates a -1 value of correlation between variables. We observe in Fig. 1 that there exists a strong correlation among features  $Z$ ,  $ev$ ,  $VER$ ,  $eff$ . Since  $eff$  has the highest correlation with  $T_f$ , we select the feature  $eff$  and remove features  $Z$ ,  $ev$ ,  $VER$  from the input space of the  $ML_T$ . This results in only six features in the input space of the  $ML_T$ , i.e.,  $\mathbf{x} = (r_{cle}, cs, en, rsla, rio, eff)$ . Next, we will compare ML regression models using the updated input space and choose the best-performing model as the  $ML_T$  for predicting the  $T_f$ .

## 2.2 Machine learning models for transformation temperature

The prepared dataset for the  $ML_T$  model could be represented as  $D_r = \{\mathbf{x}_r; T_f^{(r)}\}_{r=1}^n$  for  $n$  compositions, where  $\mathbf{x}_r$  is the set of features for the composition  $r$ . The role of ML is to map the  $d$ -dimensional vector  $\mathbf{x}_r$  into a singular scalar value  $T_f^{(r)}$  by learning a function  $g(\mathbf{x}_r)$ .

$$g : \mathbb{R}^d \rightarrow \mathbb{R}$$

Table 1: List of features considered in this work and their abbreviations

Abbreviation	Feature
$Z$	Atomic number
$rcl$	Clementi atomic radius ( $\text{\AA}$ ) [35]
$cs$	Pettifor chemical scale [36]
$en$	Pauling electronegativity [37]
$ev$	Number of valence electrons
$rsla$	Slater atomic radius [38]
$rio$	Shannon ionic radius [39]
$eff$	Electron affinity [40]
$VER$	Valence electron ratio [32]

Our goal is to predict function values  $g(\mathbf{x}^*)$  for the features  $\mathbf{x}^*$  of the unknown compositions. Some of the features in  $\mathbf{x}$  might lack having a consistent relationship with  $T_f$  and hence, they do not add any predictive value to the model’s performance. It is necessary to investigate how the inclusion of features impacts the model’s performance. We have randomly implemented a Gaussian process (GP) regression model for this study. We create six GP models, each with a subset of features as input from  $\mathbf{x}$ . The subset for each model is defined using sequential feature addition as shown in Fig 2a. The best set of features for any one of these models is obtained by best subset selection [41]. In this approach, every possible combination of features is used as input to the model and the set of features that provides the greatest improvement in performance is selected. The hyperparameters of these models are optimized using the RandomSearchCV [42] algorithm. Once we find the best-performing model among the six GP models, we use its features to compare different non-parametric ML methods.

To measure the performance of GP models, we divide the full data  $D = \bigcup_{r=1}^{44} D_r$  into 22 subsets. The GP model is repeated 22 times, each time using a unique single subset for testing and the remaining 21 subsets for training. This process is generally known as K-fold cross-validation and for our model, it is 22-fold cross-validation. The GP model predicts  $T_f$  for each testing subset, and these predictions are combined to form a single array of predicted  $T_f$  for all 44 compositions. The performance of the cross-validation is evaluated based on the error matrix root mean square error (RMSE) between the predicted  $T_f$  and actual  $T_f$  of all 44 compositions. The cross-validation is repeated 20 times to average out the variability in the performance of RMSE. The repeated cross-fold validation is plotted for all six GP models, and shown in Fig. 2b. Here, we find that the GP model with four features ( $cs$ ,  $rio$ ,  $en$ ,  $rsla$ ) has the minimum mean value of the RMSE. This highlights that the addition of features  $rcl$  and  $eff$  in the fifth and sixth GP models do not improve the mean value of RMSE. Hence we have selected the four feature model for comparing the performance of different ML methods.

There are many non-parametric ML methods available in the literature to model the structure-property relationship in materials. For example, Liu et al. [43] used various physical features (elemental, reactivity, thermal properties, and electronic structure configuration) as input to the Support Vector Regression (SVR), Random Forest (RF) and Gaussian Process (GP) model and predicted  $T_f$  of NiTiHf shape memory materials. They concluded that the GP model not only provides superior accuracy in response prediction but also estimates variance in response, i.e., uncertainty in prediction. Knowledge of uncertainty in the response prediction gives a confidence interval of prediction, which is useful in identifying a synthetic composition with confidence for future XRD experiments. Similarly, Kankanamge et al. [44] used alloy

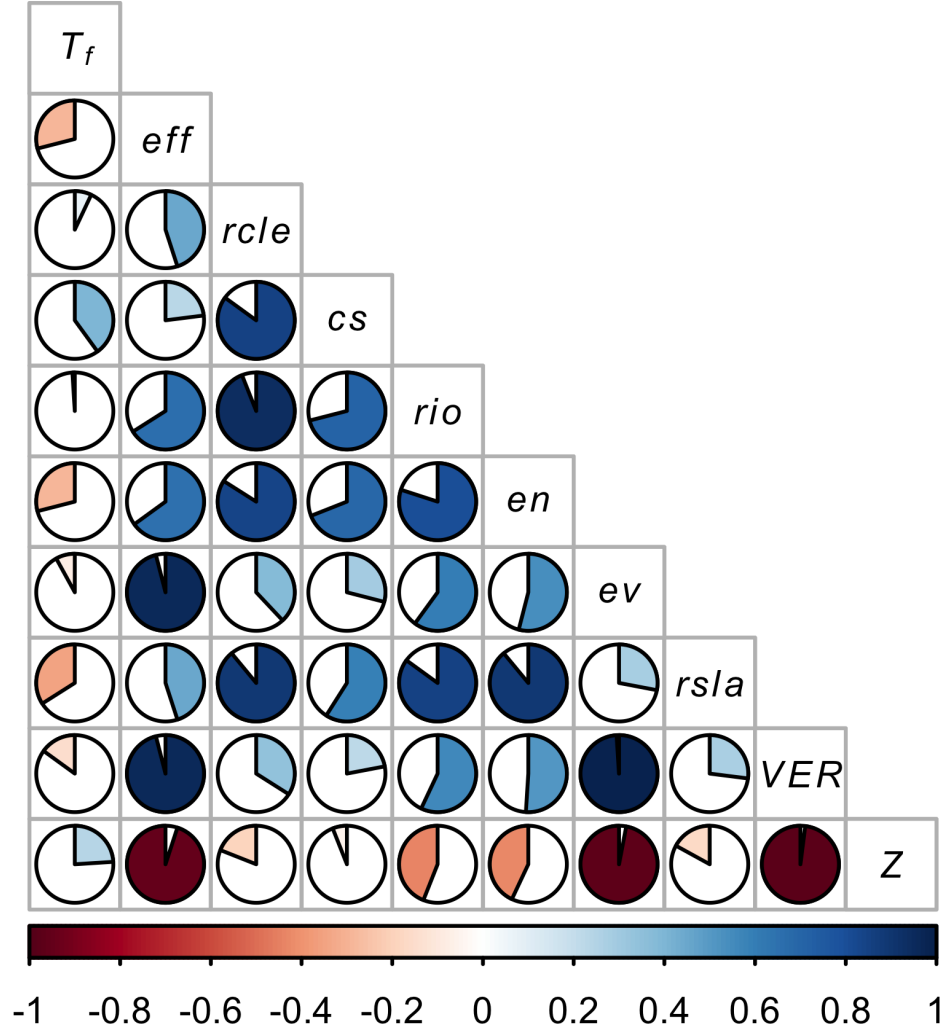


Figure 1: Pearson correlation map for physical features: This graphical map shows Pearson cross-correlation coefficient among all the initial features and indicate the relative redundancies. Many features that have strong correlation among each other can be filtered out by just choosing one feature among all.

composition of NiTiHf shape memory alloys and predicted its martensite start temperature  $M_s$  using linear, polynomial, SVR, and K-nearest neighbor (KNN) and found the KNN model to show best performance in prediction of  $M_s$ .

Based on the literature survey, we have selected the RF, KNN, and GP to compare their performance in predicting the structure-property relationship in the SMC. Each method takes the four features ( $cs$ ,  $rio$ ,  $en$ ,  $rsla$ ) as input and predicts the  $T_f$  as output. We implement the 22-fold cross-validation for each method. The training subset from the last cross-validation fold is used to check the performance in predicting training data. In this case, RF predicts with superior performance than GP and KNN. However, the performance of the ML methods on the test data is more important. The predicted  $T_f$  for each test subset of the cross-validation

are combined to measure a collective performance, and here, GP outperforms KNN and RF. The performance matrices—coefficient of determination ( $R^2$ ) and RMSE—for the training and testing data are shown in Table 2.

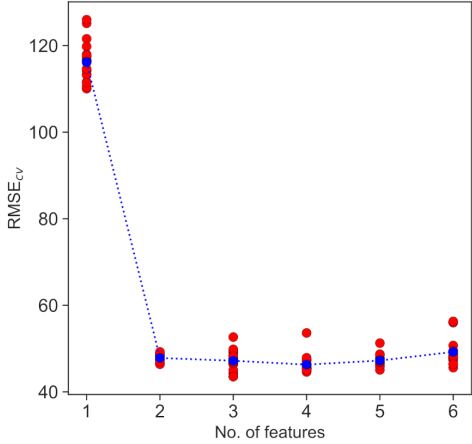
Table 2:  $R^2$  and RMSE for GP, KNN and RF

Model	$R^2$	$R^2$	RMSE	RMSE
	Train	Test	Train	Test
Gaussian Process (GP)	0.92	0.85	34.17	49.30
K-nearest neighbour (KNN)	0.87	0.77	44.72	59.60
Random Forest (RF)	0.96	0.74	22.69	62.82

The predicted  $T_f$  for all test subsets of the cross-validation are compared with the actual  $T_f$  by GP, KNN, and RF models in Fig. 3(a), (b), and (c) respectively. Ideally, the predicted data points should lie at the  $45^\circ$  line for a perfect model with  $R^2 = 1$ . However, in our case, the GP, KNN, and RF models account for 85%, 77%, and 74% of the variance observed in the actual testing data, respectively. Additionally, GP provides confidence in its prediction given the available data in terms of uncertainty. This uncertainty is known as Epistemic uncertainty, which is plotted in Fig. 3(a) as  $T_f \pm 1.96\sigma$ , and interpreted that there is a 95% chance that predicted  $T_f$  will lie in  $T_f \pm 1.96\sigma$  for any given  $x_i$ .

Feature	No. of Features					
	1	2	3	4	5	6
<i>cs</i>			x	x	x	x
<i>eff</i>	x					x
<i>en</i>		x	x	x	x	x
<i>rcle</i>					x	x
<i>rio</i>		x	x	x	x	x
<i>rsla</i>				x	x	x

(a)



(b)

Figure 2: Effect of number of input parameters on RMSE of testing data obtained by Gaussian process regression (a) Six model has been tested with specific set of features (b) RMSE of the testing data depends on the no. of features chosen in the model.

### 3 Prediction of lattice parameters

A robust ML model that predicts lattice parameters of monoclinic and tetragonal crystal structures of Zirconia-based ceramics would enable calculation of cofactor conditions [5] and identify compositions that closely satisfy cofactor conditions. The lattice parameters should be predicted with very high accuracy for close satisfaction of the cofactor conditions. We choose the GP model for prediction of both monoclinic and tetragonal crystal lattice parameters due to its ability to provide predictions as a normal distribution with uncertainty bounds. The

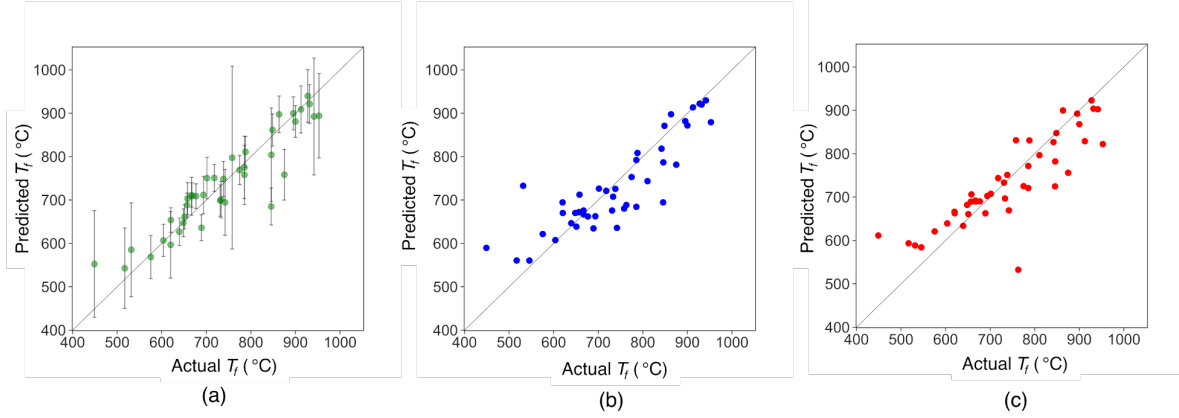


Figure 3: Performance of ML models on all test subsets: Comparison of Actual vs. Predicted  $T_f$  by (a) GP (b) KNN and (c) RF. Figure 3(a) also contains the variance or uncertainty in prediction as error bars.

GP models for the monoclinic lattice parameters is termed  $GP_m$  and for the tetragonal lattice parameters is termed as  $GP_t$ . The temperature at which lattice parameters are measured,  $T$ , strongly influences the lattice parameters [30], making it one of the key input parameters in both the  $GP_m$  and  $GP_t$ . In the next subsection, we aim to identify other key physical features as additional input parameters for the  $GP_m$  and  $GP_t$ .

### 3.1 Predictions of monoclinic crystal’s lattice parameters

In the monoclinic crystal structure, the conventional unit cell of the lattice has the lattice parameters  $a_m$ ,  $b_m$ ,  $c_m$  and the angle between them are  $90^\circ$ ,  $\beta$ ,  $90^\circ$ . The  $GP_m$  models predict the  $a_m$ ,  $b_m$ ,  $c_m$ , and  $\beta$ . We discussed that the lattice parameters have strong correlation with the feature  $T$ , hence  $T$  is considered as an input to the  $GP_m$ . For the experimental XRD data, the Pearson correlation coefficient between the lattice parameters and  $T$  is shown in Table 3. Here, we observe that the lattice parameters  $a_m$ ,  $c_m$  and  $\beta$  have strong correlation with  $T$ , however  $b_m$  has weak correlation with  $T$ . This signifies that  $T$  alone is not a sufficient input to the  $GP_m$  for high accuracy in prediction of  $b_m$ . Thus, we consider including addition physical features from Fig. 2a in the input space of the  $GP_m$ . The relevant features necessary for high accuracy of the  $GP_m$  are identified based on features selection study to predict  $b_m$ .

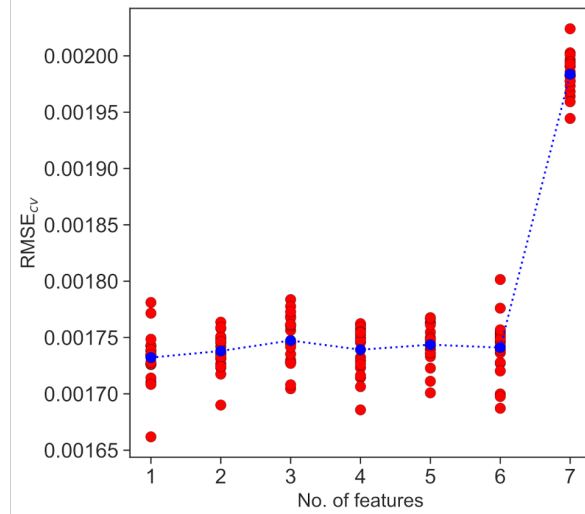
Table 3: Pearson correlation coefficient between  $T$  and lattice parameters

	$a_m$	$b_m$	$c_m$	$\beta$	$a_t$	$c_t$	$T$
$T$	0.92	-0.07	0.86	-0.82	0.92	0.61	1

In the feature selection study, our goal is to identify key physical features among seven features ( $T$ ,  $rcl$ ,  $cs$ ,  $en$ ,  $rsl$ ,  $rio$ ,  $eff$ ) to represent the input space of GP models to predict  $b_m$ . For this study, seven GP models are created, with the first one having only one feature and each subsequent model having an additional single increment in the number of features, as shown in Fig. 4a. The best input features for a model are obtained by the best subset selection. For each model, 20-fold cross-validation is performed, which is repeated 20 times, and plotted in Fig. 4b. We observe that the mean value of  $RMSE_{cv}$  does not significantly change by including up to 4 features i.e.,  $eff$ ,  $rcl$ ,  $cs$ ,  $rio$ . The GP model with 4 features also gives the least variance in the  $RMSE_{cv}$  value among all 7 GP models, marking its features as

Feature	No. of Features						
	1	2	3	4	5	6	7
<i>cs</i>			x	x	x	x	x
<i>eff</i>			x	x	x	x	x
<i>en</i>					x	x	x
<i>rcl</i>		x	x	x	x	x	x
<i>rio</i>		x		x	x	x	x
<i>rsla</i>	x					x	x
<i>T</i>							x

(a)



(b)

Figure 4: Effect of no. of input parameters on RMSE of testing data obtained by GP regression (a) Seven GP regression models with best subset of features for prediction of lattice parameters  $b_m$  (b) RMSE of the testing data depends on the no. of features.

the best subset.

It makes physical sense to use the same subset to predict the lattice parameters of the monoclinic crystal structure. We also include the  $T$  in the current subset because the lattice parameters  $a_m$ ,  $c_m$  and  $\beta$  have a strong correlation with the  $T$ . Thus, the features in the updated subset ( $T$ ,  $eff$ ,  $rcl$ ,  $cs$ ,  $rio$ ) are used as input parameters to predict all monoclinic lattice parameters. The lattice parameters  $a_m$ ,  $b_m$ ,  $c_m$  and  $\beta$  are taken as output individually during training the GP models. The predictions of lattice parameters  $a_m$ ,  $b_m$ ,  $c_m$  and  $\beta$  are shown in Fig. 5a, b, c, and d respectively.

### 3.2 Predictions of tetragonal crystal's lattice parameters

In the tetragonal crystal structure, the conventional unit cell of the lattice has the lattice parameters  $a_t = b_t$  and  $c_t$ . The angle between them are all  $90^\circ$ . The  $GP_t$  models predict the  $a_t$  and  $c_t$  respectively. In order to identify key physical features as input parameters in the  $GP_t$  model, the feature selection study is conducted. Our goal is to identify key physical features among seven features ( $T$ ,  $rcl$ ,  $cs$ ,  $en$ ,  $rsla$ ,  $rio$ ,  $eff$ ) to represent the input space of the  $GP_t$  model. We follow similar steps for the feature selection study as explained for the monoclinic lattice parameters. Seven GP models are created, each with increasing no. of features, as shown in Fig. 6a. The lattice parameter  $c_t$  is predicted from the seven GP models. This is because  $c_t$  has a relative weaker correlation of 0.61 with  $T$  compared to the lattice parameter  $a_t$ , which has a correlation of 0.92 with  $T$ , as shown in Table 3.

The mean value of the RMSE of the 20 times repeated 20-fold cross validation does not significantly change after including 4 features ( $T$ ,  $eff$ ,  $cs$ ,  $en$ ) in the model, as shown in Fig. 6b. The features that provide high efficiency in the prediction of the lattice parameter  $c_t$  are likely to be informative for predicting the lattice parameter  $a_t$ . Thus, it makes physical sense to use these four features as input for prediction of both the  $a_t$  and  $c_t$  individually by the  $GP_t$ . The

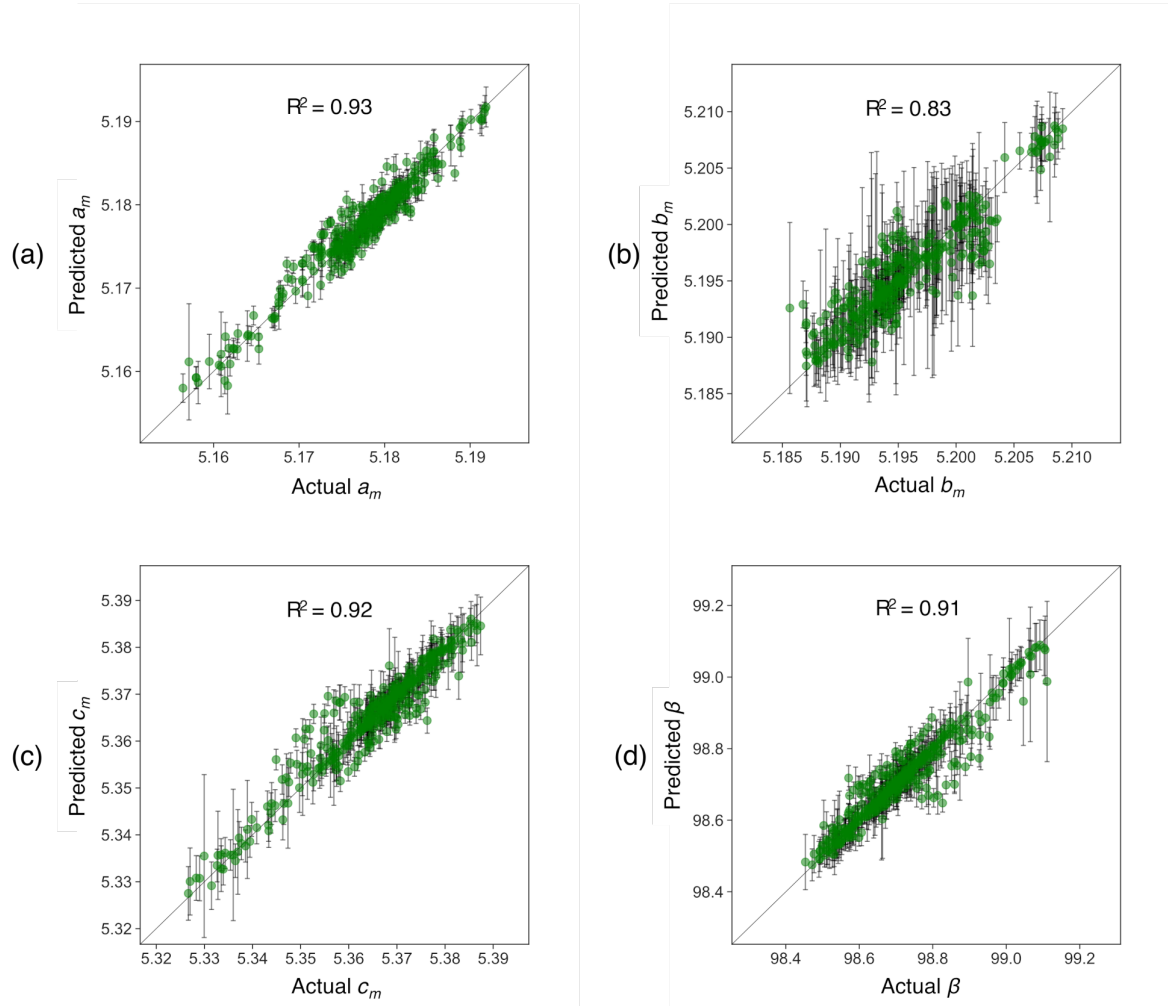


Figure 5: Predicted vs. actual values of monoclinic crystal's lattice parameters: (a)  $a_m$  (b)  $b_m$  (c)  $c_m$  (d)  $\beta$ .

predictions from all the testing sets of the cross-fold validation are combined and compared with actual XRD measurements in Fig. 7.

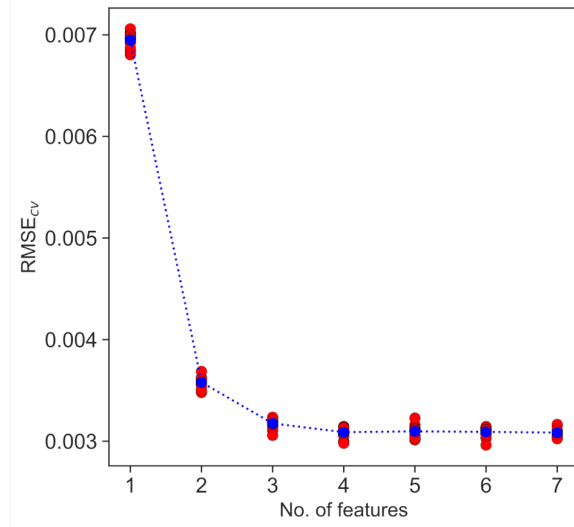
## 4 Theory of reversibility of phase transformation

In this section, we review conditions of compatibility between the phases with regard to reversibility and hysteresis of phase transformation. These conditions are purely geometric and depends only on the crystal structure and lattice parameters of the two phases. These conditions influence the stress in transition layers and the heights of energy barriers that relate to hysteresis. We will describe two conditions of supercompatibility,  $\lambda_2 = 1$  and the *cofactor conditions*.

The *transformation stretch matrix* and the two groups that represent the point group symmetries of the two phases, are the terms used to express the two conditions of supercompatibility. In order to define the transformation stretch matrix, we first observe that in the most reversible martensitic phase transformations, the point group symmetries of the two

Feature	No. of Features						
	1	2	3	4	5	6	7
<i>cs</i>				x		x	x
<i>eff</i>	x	x	x	x	x	x	x
<i>en</i>			x	x	x	x	x
<i>rcle</i>							x
<i>rio</i>					x	x	x
<i>rsla</i>					x	x	x
<i>T</i>		x	x	x	x	x	x

(a)



(b)

Figure 6: Study of feature selection for the tetragonal lattice parameters: (a) Seven GP models, each with best features for minimizing RMSE (b) RMSE of the testing data depends on the no. of selected features.

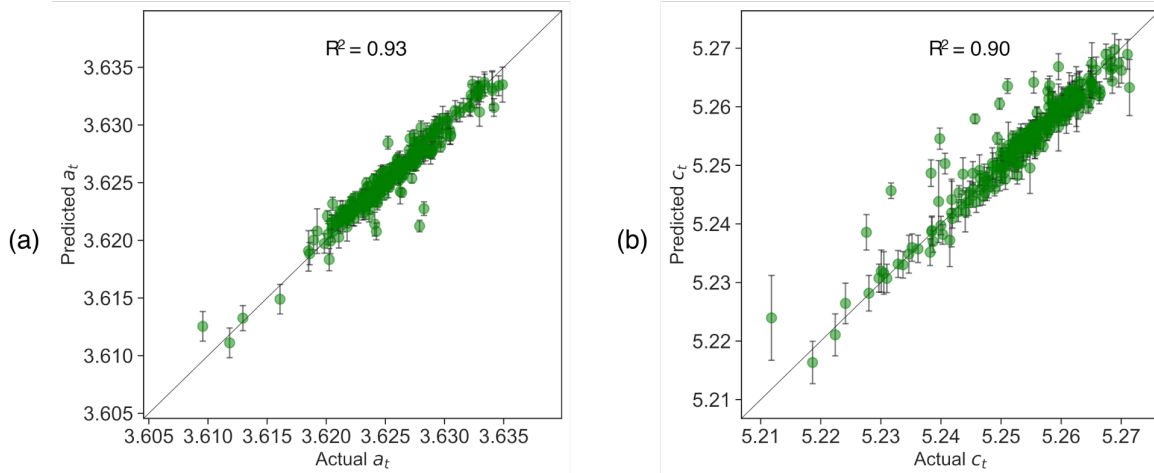


Figure 7: Predicted vs. actual values of tetragonal crystal's lattice parameter (a)  $a_t$  (b)  $c_t$

phases have a group–subgroup relation. The point group of the low temperature phase is a subgroup of the point group of the high temperature phase. Hence, there exists a primitive lattice describing the periodicity of the martensite crystal, as delineated by vectors  $\mathbf{b}_1$ ,  $\mathbf{b}_2$ ,  $\mathbf{b}_3$ , and a sublattice of the austenite with periodicity  $\mathbf{a}_1$ ,  $\mathbf{a}_2$ ,  $\mathbf{a}_3$  exhibiting about the same unit-cell volumes. During phase transformation, the martensite primitive lattice is deformed from the austenite sublattice through a linear transformation  $\mathbf{F}$  ( $\det \mathbf{F} \neq 0$ ) such that  $\mathbf{b}_i = \mathbf{F}\mathbf{a}_j$ . If  $\mathbf{F}$  is assumed to have positive determinant by changing sign of one of the vectors, then,  $\mathbf{F}$  has a polar decomposition  $\mathbf{F} = \mathbf{R}\mathbf{U}$ , where  $\mathbf{R}$  is a  $3 \times 3$  rotation matrix, and  $\mathbf{U}$  is the *transformation stretch matrix*, which is positive definite and symmetric.

The primitive lattice of the martensite may have about the same unit cell volume as several sublattices of the austenite. Based on study by Bain [45] and Lomer [46], it is observed

that given the sublattice of the austenite  $\mathbf{a}_1, \mathbf{a}_2, \mathbf{a}_3$ , the material often chooses the primitive lattice of martensite which gives the smallest strain  $\|\mathbf{U} - \mathbf{I}\|$ , measured in a suitable norm. Chen et al. [5] and Koumatos et al. [47] describe suitable algorithms for calculating  $\mathbf{U}$  based on this principle. This procedure shares a close relationship with the widely used *Cauchy-Born rule*. This rule is used to link atomic level deformations to macroscopic deformation. A continuous deformation  $\mathbf{y}(\mathbf{x})$  defined on a domain  $\Omega$  has a gradient that takes the value  $\nabla\mathbf{y}$ . The interpretation of this rule is,  $\mathbf{F} = \nabla\mathbf{y}$  represents the macroscopic deformation gradient.

The  $\mathbf{U}$  has three real eigenvalues  $0 < \lambda_1 \leq \lambda_2 \leq \lambda_3$ , since it is positive definite and symmetric. Among these eigenvalues,  $\lambda_2$  is of particular importance because of the following theorem [15] (Prop. 4): *a necessary and sufficient condition that a continuous deformation  $\mathbf{y}(\mathbf{x})$  defined on a domain  $\Omega$  has a gradient that takes value  $\nabla\mathbf{y} = \mathbf{F} = \mathbf{R}\mathbf{U}$  (martensite) on a region  $\mathcal{R}$  and  $\nabla\mathbf{y} = \mathbf{I}$  (austenite) on the complementary region  $\Omega \setminus \mathcal{R}$  for some rotation matrix  $\mathbf{R}$  is that  $\lambda_2 = 1$ . To relate this statement to Prop. 4 of [15], note that  $\mathbf{y}(\mathbf{x})$  of this form is continuous if and only if  $\mathbf{F} = \mathbf{R}\mathbf{U} = \mathbf{I} + \mathbf{b} \otimes \mathbf{m}$  for some vectors  $\mathbf{b}$  and  $\mathbf{m}$ . The vector  $\mathbf{m}$  is taken as normal to the interface between the austenite and the martensite and the vector  $\mathbf{b}$  is the shape strain vector. We take  $\mathbf{F}^T \mathbf{F}$  to eliminate the rotation matrix  $\mathbf{R}$  and note that the eigenvalues of  $\mathbf{C} = \mathbf{F}^T \mathbf{F}$  are the squares of the eigenvalues of the positive definite, symmetric matrix  $\mathbf{U}$  so, in particular,  $\mathbf{U}$  has middle eigenvalue equal to 1 if and only if  $\mathbf{C} = \mathbf{F}^T \mathbf{F}$  has the middle eigenvalue equal to 1.*

The compatibility condition  $\lambda_2 = 1$  strongly affects hysteresis [3, 48, 1, 2], and improves reversibility under thermal cycling [3]. A detailed theory of influence of geometric condition on hysteresis is given in [2]. The summary of the theory is as follows. This is observed in both theory [49] and experiment [50] that a well-developed nuclei of martensite exist above the austenite finish temperature  $A_f$ . The theory [2], based on a concept of metastability, hypothesizes that lowering the temperature below that at which two bulk phases have the same free energy leads to growth of a twinned platelet. During small undercooling, a spontaneous thickening of the platelet results in an increase in energy. This is attributed to the subtle interplay between bulk and interfacial energy at the twinned austenite/martensite interfaces that bind the platelet. The bulk energy dominates at sufficiently large sizes of the platelet, and growth of the platelet leads to a decrease in the energy with size. The large-scale transformation is caused at a certain under-cooling when a sufficient number of nuclei have a size beyond the barrier.

The delicate interplay between bulk and interfacial energy at the austenite/martensite interface is the main reason why  $\lambda_2$  so strongly affects hysteresis. At  $\lambda_2 = 1$ , the existence of a perfectly unstressed interface between phases implies that the elastic energy in the stressed transition layer is eliminated. As  $\lambda_2$  departs from 1, and particularly in the case when  $\lambda_2 > 1$ , the bulk energy in the transition layer grows extremely rapidly. When this theory is applied to cubic to orthorhombic transformations in TiNiX alloys, a graph of hysteresis vs.  $\lambda_2$  is observed similar to that shown in Fig. 8. A very sharp drop in hysteresis is observed near  $\lambda_2 = 1$  as shown in Fig. 8(b).

#### 4.1 Cofactor conditions

The cofactor conditions [5][4] consist of three conditions (i) the compatibility condition  $\lambda_2 = 1$  discussed above (ii) a second condition that depends on the twin system chosen, and (iii) an inequality that is satisfied for Type-I or Type-II twin system. In this section, we discuss meaning of satisfying (ii) only.

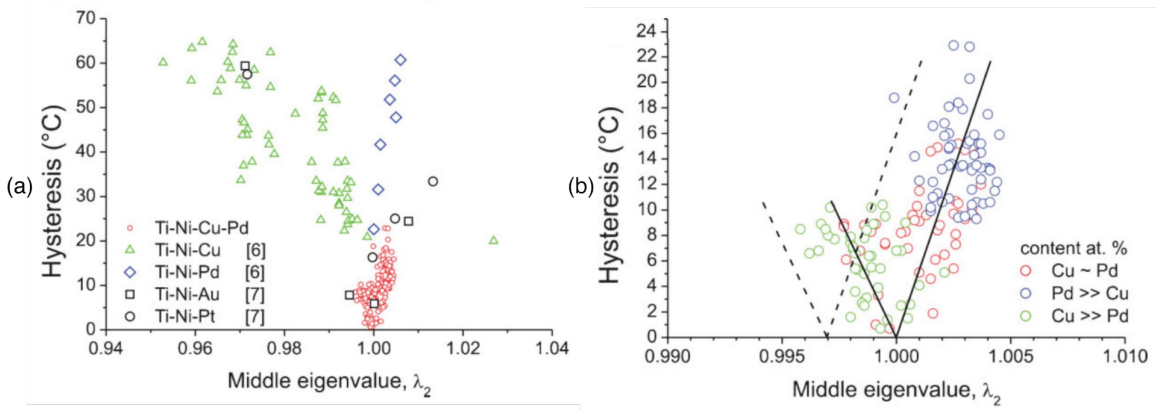


Figure 8: Measurements for alloys in Ti-Ni-X system (a) Hysteresis vs  $\lambda_2$  (b) Closeup of graph in (a) near  $\lambda_2 = 1$ , taken from [3].

The cofactor conditions are derived from the crystallographic theory of martensite [51] [18]. The ubiquitous austenite/twinned martensite interface ("habit plane") in martensitic phase transformation is governed by this theory. By refining the twins, it provides necessary and sufficient conditions for the bulk energy in the elastic transition layer between phases to become vanishingly small. This theory has as unknowns the volume fraction  $f$  of twins in the laminate of the martensite phase defined on the domain  $\Omega$ , a rigid body rotation  $\mathbf{R}_f$  of the austenite, a unit normal to the habit plane  $\mathbf{m}$  and a shear vector  $\mathbf{b}$  [15]. We summarize the theory in brief and say that the domain  $\Omega$  has a martensite laminate with the twin structure. Let's say that the twin structure has two variants of the martensite, where  $\mathbf{R}_1\mathbf{U}_j$  represents one of the variants of the martensite, and the other variants is represented by  $\mathbf{R}_2\mathbf{U}_i$ . For the deformation  $\mathbf{y}(\mathbf{x})$  to be continuous in the twin laminate, it is necessary that the deformation gradient of the martensite variants i.e.,  $\mathbf{R}_1\mathbf{U}_j$  and  $\mathbf{R}_2\mathbf{U}_i$  satisfy  $\mathbf{R}_1\mathbf{U}_j - \mathbf{R}_2\mathbf{U}_i = \mathbf{a} \otimes \mathbf{n}$ . The interface between the two region is a plane with reference normal  $\mathbf{n}$ , and  $\mathbf{a}$  is the twinning shear vector. This condition is known as kinematic compatibility condition.

If  $f$  represents the total volume fraction of the variant with deformation gradient  $\mathbf{R}_1\mathbf{U}_j$ , then  $(1 - f)$  represents the total volume fraction of the variant with the deformation gradient  $\mathbf{R}_2\mathbf{U}_i$ . The average deformation gradient for the martensite laminate is  $\mathbf{F}_{\text{avg}} = f\mathbf{R}_1\mathbf{U}_j + (1 - f)\mathbf{R}_2\mathbf{U}_i$ . The polar decomposition of the  $\mathbf{F}_{\text{avg}} = \mathbf{R}_f\mathbf{U}_f$ , where  $\mathbf{R}_f$  is the rotation of the austenite and  $\mathbf{U}_f$  is the average transformation stretch matrix. The deformation  $\mathbf{y}(\mathbf{x})$  defined on the domain  $\Omega$  is continuous if and only if  $\mathbf{R}_f\mathbf{U}_f = \mathbf{I} + \mathbf{b} \otimes \mathbf{m}$ . Note that the eigenvalues of  $\mathbf{C}$  are the squares of the eigenvalues of the positive-definite, symmetric matrix  $\mathbf{U}_f$ . Now,  $\mathbf{U}_f$  has the middle eigenvalue  $\lambda_2 = 1$  if and only if  $\mathbf{C} = \mathbf{F}_{\text{avg}}^T\mathbf{F}_{\text{avg}} = \mathbf{U}_f^T\mathbf{U}_f$  has the middle eigenvalue equal to 1. This implies that one of the roots of the characteristic polynomial  $\det(\mathbf{C} - \mathbf{I})$  must be zero, which is  $(\lambda_2^2 - 1) = 0$ .

This implies that the theory reduces to a single scalar equation  $\det(\mathbf{C} - \mathbf{I}) = 0$  for the volume fraction  $f$ . (See Theorem 2 of [5] for the definition of  $\mathbf{C}$ .) It turns out [15] that in all cases,  $\det(\mathbf{C} - \mathbf{I}) = 0$  is a quadratic equation for  $0 \leq f \leq 1$ . There are various possibilities of this quadratic function, as seen in Fig. 9. It can have no real root, as seen in Fig. 9a. Many martensitic steel (but not all) has non-reversible martensite, with Fig. 9a holds for all twin system. Or, It can have exactly two roots  $f^*$  and  $1 - f^*$  as shown in Fig. 9b: many NiTi-based or Cu-based shape memory alloys satisfy this classic case. Also, a mild inequality must be satisfied for these roots to give a solution. If it holds, then among these two roots, there are

two interfaces corresponding to  $f^*$  and two interfaces corresponding to  $1 - f^*$  i.e., four solution per twin system as shown in Fig. 9(top, right). If these two roots  $f^*$  and  $1 - f^*$  occurs at 0 and 1, as shown in Fig. 9c, and again if a certain inequality holds, this is the situation we discussed in the section 4 above for the compatibility condition  $\lambda_2 = 1$ . The four possible interfaces are shown to the right of Fig 9c. Finally, if the quadratic function is identically zero for all values of  $f$  as shown in Fig. 9d, then these conditions are called *cofactor conditions*. Assuming again a certain inequality is usually satisfied, this means that there exist low energy interfaces for any volume fraction  $0 \leq f \leq 1$  of the twins.

There are hosts of implications of satisfying the cofactor conditions [5]. Satisfaction of cofactor conditions for one twin system implies its satisfaction for other crystallographic twin system. Also, the solution of the crystallographic theory for Types I and II twin system exist with no elastic transition layer, platelet nucleation mechanism with zero elastic energy, and complex "riverine" zero energy microstructure [19]. There are strong correlations [52] that relates the satisfaction of cofactor condition to reversibility. These correlations are possible on satisfaction of cofactor condition due to many strain and many interfaces possible in low (or zero)-energy microstructure involving both austenite and martensite.

The quadratic function  $q(f) = \det(\mathbf{C} - \mathbf{I})$  vanishes identically if and only if  $q(0) = 0$  and  $q'(0) = 0$ . In terms of the twin system  $\mathbf{a}$ ,  $\mathbf{n}$  (Types I and II) and transformation stretch matrix  $\mathbf{U}$ , the cofactor conditions [5] are:

$$\begin{aligned} q(0) = 0 &\longleftrightarrow \lambda_2 = 1 \\ q'(0) = 0 &\longleftrightarrow \mathbf{a} \cdot \mathbf{U}_i \text{cof}(\mathbf{U}_i^2 - \mathbf{I})\mathbf{n} \\ &= 0, \text{CCI (for Type I twin) or CCII (for Type II twin)} \\ \text{tr}\mathbf{U}_i^2 - \det\mathbf{U}_i^2 - \frac{\mathbf{a}^2\mathbf{n}^2}{4} - 2 &\geq 0 \end{aligned}$$

The latter is an inequality referred to above. It is satisfied for all Types I and II twin system.

## 4.2 Multiple transformation correspondences

In tetragonal to monoclinic phase transformation, Kelly et. al. [53] pointed out the presence of three types of correspondences, which describes how the basis vectors of the tetragonal lattice are mapped to the monoclinic lattice. These correspondences are also noticed by Hayakawa et. al. [54][55] in  $\text{ZrO}_2\text{-Y}_2\text{O}_3$  system, and by Pang et. al. [56] in  $\text{ZrO}_2\text{-CeO}_2$  ceramics for the tetragonal to monoclinic transformation.

For each of the correspondences obtained by mapping the tetragonal to monoclinic basis vectors, there are four variants of martensite, which is defined by the point group relationship of the tetragonal and monoclinic lattices. For the basis vectors  $\mathbf{a}_i$  of the tetragonal lattice, its point group  $\mathcal{P}(\mathbf{a}_i)$  is the set of rotations that maps the lattice back to itself. Thus,  $\mathcal{P}(\mathbf{a}_i) = \{\mathbf{R} \in \text{SO}(3) : \mathbf{R}$  is a rotation and  $\mathbf{R}\mathbf{a}_i = \mu_i^j\mathbf{a}_j$  for  $\mu_i^j$  (a  $3 \times 3$  matrix) satisfying  $\det(\mu_i^j) = \pm 1\}$ . It is reasonable to assume that the point group of the martensite basis  $\mathbf{b}_i$ , given by  $\mathcal{P}(\mathbf{b}_i)$ , is a subgroup of the point group of the austenite [7]. The group-subgroup relationship between the austenite and the martensite gives rise to symmetry-related variants of the martensite. The relationship between variant  $i$  with the transformation stretch tensor  $\mathbf{U}_i$  and variant  $j$  with transformation stretch tensor  $\mathbf{U}_j$  is

$$\mathbf{U}_j = \mathbf{R}\mathbf{U}_i\mathbf{R}^T, \quad (3)$$

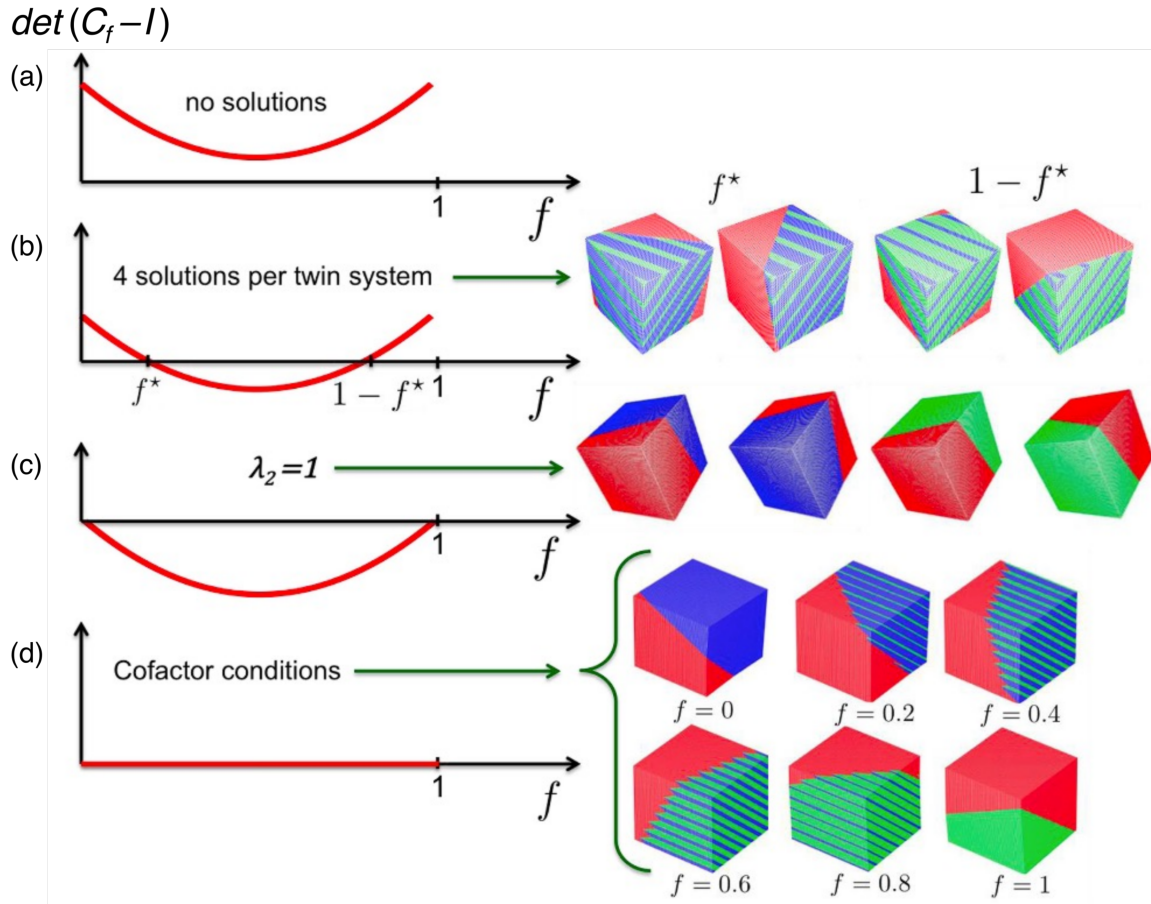


Figure 9: In the context of the crystallographic theory of martensite, the meaning of cofactor condition is: (a) No roots of the  $\det(\mathbf{C} - \mathbf{I})$  leading to no solution for the given twin system (b) the generic case of 4 solution per twin system satisfied by many reversible martensites (c) the case  $\lambda_2 = 1$  (d) the cofactor conditions are exactly satisfied (The accompanying illustration depicts an example of type-I twins). Color code: blue and green are variants of martensite, and red is austenite.

Where  $\mathbf{R}$  is in the point group of austenite but not in the point group of martensite. For the tetragonal to monoclinic phase transformation, we express it as  $\mathbf{R} \in \mathcal{P}^{\text{tet}}/\mathcal{P}^{\text{mono}}$ . The number of rotations in the point group is called the order of that group. The number of variants for tetragonal to monoclinic transformation is given by the ratio of the order of the point group of austenite to the order of the point group of martensite. The tetragonal crystal has an order of 8 in its point group and the monoclinic crystal has an order of 2 in its point group. The ratio  $8/2$  gives a total of 4 variants of the martensite.

There are three distinct correspondences ( $1_a$ ,  $1_b$  and 2) for tetragonal to monoclinic transformation, each having four variants of martensite. The correspondences  $1_a$ ,  $1_b$  and 2 are denoted as correspondences C, A and B respectively in Kelly's notation. In correspondence- $1_b$ , the tetragonal 4-fold  $c_t$  axis in  $[0\ 0\ 1]$  deforms to the monoclinic  $a_m$  axis as shown in Fig. 10b. In correspondence-2, the tetragonal 4-fold  $c_t$  axis transformed to the monoclinic two-fold  $b_m$  axis, as shown in Fig. 10c. The deformation of tetragonal 4-fold  $c_t$  axis in  $[0\ 0\ 1]$  to the monoclinic  $c_m$  axis generates the correspondence- $1_a$ , as shown in Fig. 10d.

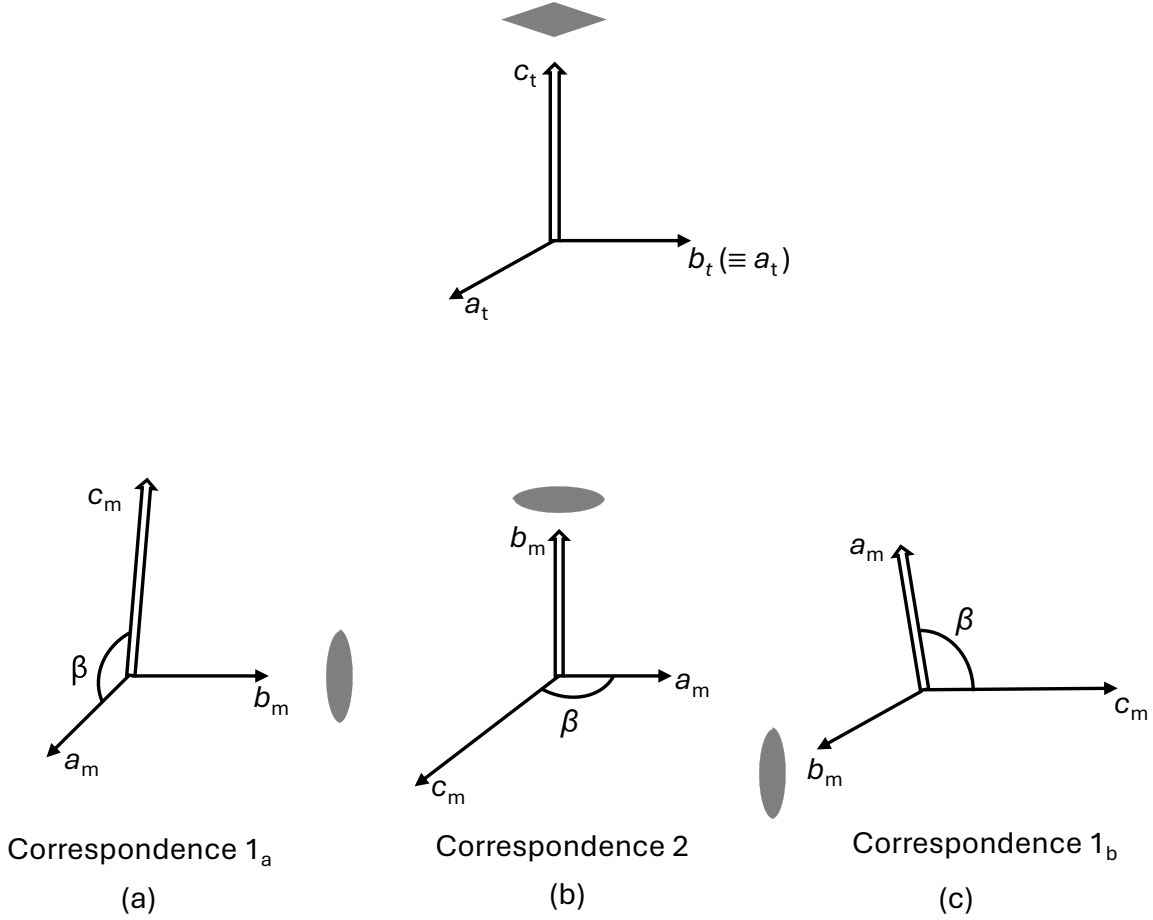


Figure 10: The tetragonal crystal in (a) transforms to a monoclinic crystal so that the  $c_t$  axis becomes: (b)  $a_m$  axis of correspondence 1<sub>b</sub> (c)  $b_m$  axis of correspondence 2 (d)  $c_m$  axis of correspondence 1<sub>a</sub>. The gray lens denotes the four fold symmetry axis in tetragonal crystal and two fold symmetry axis in monoclinic crystal.

Each one of the correspondences has four variants. For example, the 4 stretch matrices of variants for the correspondence 2 are as follows:

$$\mathbf{U}_1 = \begin{bmatrix} a & d & 0 \\ d & b & 0 \\ 0 & 0 & c \end{bmatrix}, \mathbf{U}_2 = \begin{bmatrix} b & d & 0 \\ d & a & 0 \\ 0 & 0 & c \end{bmatrix}, \mathbf{U}_3 = \begin{bmatrix} a & -d & 0 \\ -d & b & 0 \\ 0 & 0 & c \end{bmatrix}, \mathbf{U}_4 = \begin{bmatrix} b & -d & 0 \\ -d & a & 0 \\ 0 & 0 & c \end{bmatrix} \quad (4)$$

The unknowns  $a$ ,  $b$ ,  $c$  and  $d$  are functions of the lattice parameters of the both phases  $a_m$ ,  $b_m$ ,  $c_m$ ,  $\beta$ ,  $a_t$  and  $c_t$ . Similarly, the correspondence-1<sub>a</sub> and correspondence-1<sub>b</sub>, each has 4 variants. The form of stretch matrices of these correspondences and the information about the unknowns  $a$ ,  $b$ ,  $c$ , and  $d$  are given in the supplementary section 1-3 of Hanlin et. al. work on correspondences [6].

Any variant from one correspondence could form a compatible interface with the variants of the other two correspondences in the martensite twin structure. However, the energy in the transition layer should be made arbitrarily small if they are compatible. Hanlin et. al.

calculated the number of compatible laminated martensite/austenite interfaces and showed them in the tables of supplement [6]. They observed that a twin structure with selected variants from correspondence-1<sub>a</sub> and correspondence-2 i.e., ( $\mathbf{U}_i^{(1a)}/\mathbf{U}_j^{(2)}$ ) or from correspondence-1<sub>b</sub> and correspondence-2 i.e., ( $\mathbf{U}_i^{(1b)}/\mathbf{U}_j^{(2)}$ ) or from both correspondences-2 i.e., ( $\mathbf{U}_i^{(2)}/\mathbf{U}_j^{(2)}$ ) is favored compared to unmixed correspondences ( $\mathbf{U}_i^{(1a)}/\mathbf{U}_j^{(1a)}$ ;  $\mathbf{U}_i^{(1b)}/\mathbf{U}_j^{(1b)}$  and  $\mathbf{U}_i^{(1a)}/\mathbf{U}_j^{(1b)}$ ).

Our ceramic system has a new dopant  $\text{Er}_2\text{O}_3$ , compared to previously conducted studies on compositions [6, 25, 56], where  $\text{Er}_2\text{O}_3$  doping is absent. For our ceramic system, we found that variants, both from correspondence  $\mathbf{U}^{(1a)}/\mathbf{U}^{(1a)}$  are compatible, but the laminate interface with correspondences  $\mathbf{U}^{(1b)}/\mathbf{U}^{(1b)}$  and  $\mathbf{U}^{(1a)}/\mathbf{U}^{(1b)}$  are not compatible. Thus, the laminated structure with the compatible variants  $\mathbf{U}_i$  and  $\mathbf{U}_j$  from any two correspondences could have one of the following combinations:

$$\mathbf{U}_i^{(2)}/\mathbf{U}_j^{(2)}, \mathbf{U}_i^{(1a)}/\mathbf{U}_j^{(2)}, \mathbf{U}_i^{(1b)}/\mathbf{U}_j^{(2)}, \mathbf{U}^{(1a)}/\mathbf{U}^{(1a)} \mid i, j \in \{1, 2, 3, 4\} \quad (5)$$

However, for any unexplored dopant addition in the ceramic system, variants from the correspondences  $\mathbf{U}^{(1b)}/\mathbf{U}^{(1b)}$  and  $\mathbf{U}^{(1a)}/\mathbf{U}^{(1b)}$  could become compatible at the twin interface of the martensite.

### 4.3 Identification of shape memory ceramics with low hysteresis

The exact satisfaction of the cofactor condition  $q(f) = \det(\mathbf{C} - \mathbf{I})$  implies that  $q(f)$  vanishes identically if and only if  $q(0) = 0$  and  $q'(0) = 0$ . On checking the cofactor conditions for various lattice parameters, it was found that they are not exactly satisfied for any composition, however, they could be considered approximately satisfied at certain compositions. The approximate satisfaction of the cofactor condition is based on a criteria of minimizing the maximum deviation from the exact satisfaction of the cofactor condition. This would physically mean that the free energy of transition layer between the laminate and the austenite can be made small. A suitable measure of this energy is the maximum deviation from the exact satisfaction of the cofactor condition. This deviation is measured as the maximum value of the quadratic function  $|q(f)|$  for values of  $f$  between 0 and 1. The composition with lattice parameters giving the minimum value of the maximum deviation is a potential sample  $i$  having low hysteresis. Thus, the new criterion based on the approximate satisfaction of the cofactor condition is:

$$h_i := \min_{\text{sample } i} \left( \max_{0 \leq f \leq 1} |q^{(i)}(f)| \right)$$

For example, there have been efforts to find correlation between phase compatibility and efficient energy conversion in Zr-doped Barium Titanate  $\text{Ba}(\text{Ti}_{1-x}\text{Zr}_x)\text{O}_3$  having cubic to tetragonal transformation. The lattice parameters are tuned by changing doping levels of Zirconia ( $x \leq 0.027$ ). The tuning of lattice parameters in  $\text{Ba}(\text{Ti}_{1-x}\text{Zr}_x)\text{O}_3$  for improved crystallographic compatibility, gives significant improvement of transformation and ferroelectric energy conversion properties [21]. These lead-free piezoceramics show that a close satisfaction of cofactor condition (with  $q(f)$  almost zero for all values of  $f$  and  $h_i = 1.75e^{-8}$ ) at mole fraction  $x = 0.017$  reduces hysteresis to  $\Delta T = 3.93 \text{ K}$  in cubic to tetragonal transformation. The middle eigenvalue value is found to be very close to 1 with  $\lambda_2 = 0.9991$ .

The new criteria could also be applied to Zirconia-based shape memory ceramics having tetragonal to monoclinic phase transformation. The presence of correspondences 1<sub>a</sub>,

2 and 1<sub>b</sub> in phase transformation of these materials creates a possibility of twin structure in martensite laminate having stretch matrices from multiple correspondences i.e.,  $\mathbf{U}_i^{(2)}/\mathbf{U}_j^{(2)}$  or  $\mathbf{U}_i^{(1a)}/\mathbf{U}_j^{(2)}$  or  $\mathbf{U}_i^{(1b)}/\mathbf{U}_j^{(2)}$ . The case in which the twin structure contains variants only from the correspondence 2 is  $\mathbf{U}_i^{(2)}/\mathbf{U}_j^{(2)}$  with the kinematic compatibility equation  $\mathbf{R}_1\mathbf{U}_j^{(2)} - \mathbf{R}_2\mathbf{U}_i^{(2)} = \mathbf{a} \otimes \mathbf{n}$ . For this case, the quadratic function  $q(f)$  is symmetric about  $f = 0.5$  with the maximum deviation value  $h_i$  appearing either at  $f = 0$  or  $f = 0.5$  or  $f = 1$ . This symmetry arises from the fact that the variants in  $\mathbf{U}_i^{(2)}/\mathbf{U}_j^{(2)}$  are symmetry related. The twin structure with different correspondences i.e,  $\mathbf{U} \in \{\mathbf{U}_i^{(1a)}/\mathbf{U}_j^{(2)}, \mathbf{U}_i^{(1b)}/\mathbf{U}_j^{(2)}\}$ , the  $q(f)$  is no longer symmetric, and has maximum deviation  $h_i$  could appear at any value  $0 \leq f \leq 1$ .

## 5 Analysis of compositions

### 5.1 Synthetic compositions and prediction of its properties

The generation of synthetic compositions plays a key role in identifying new compositions with tuned lattice parameters that satisfy the cofactor conditions. In any synthetic composition, bounding the mole fraction values of its oxides between the minimum and maximum values used in the sample preparation process is crucial for the ML models to predict the lattice parameters of the synthetic composition accurately. Thus, during generation of the compositions, the mole fraction value of each oxide  $(\text{ZrO}_2)_{m_1}$ ,  $(\text{HfO}_2)_{m_2}$ ,  $(\text{Er}_2\text{O}_3)_{m_3}$  and  $(\text{Y}_{0.5}\text{Ta}_{0.5}\text{O}_2)_{m_4}$  are bounded as  $0.1675 \leq m_1 \leq 0.71$ ,  $0.1675 \leq m_2 \leq 0.5677$ ,  $0.0 \leq m_3 \leq 0.055$  and  $0.025 \leq m_4 \leq 0.175$ . To generate the synthetic compositions, the mole fraction value of  $(\text{ZrO}_2)_{m_1}$  is incremented in steps of 0.1% starting at  $m_1 = 0.1675$  and incremented up to  $m_1 = 0.71$ . For each value of the  $m_1$ , the mole fraction of  $(\text{Y}_{0.5}\text{Ta}_{0.5}\text{O}_2)_{m_4}$  is incremented in steps of 0.1% and for each value of  $m_4$ ,  $(\text{Er}_2\text{O}_3)_{m_3}$  is incremented in steps of 0.5%. This iterative process would generate a total of 5416 synthetic compositions.

We derive physical features  $\mathbf{x}^* = (cs, rio, en, rsla)$  for the synthetic compositions using Eq. 1 and predict its transformation temperature  $T_f^*$  using  $\mathbf{x}^*$  as input of the GP model described in section 2.2. For each  $\mathbf{x}^*$ , the GP model predicts a probability distribution  $p(T_f^*|\mathbf{x}^*, \mathbf{x}, T_f) \sim \mathcal{N}(\mu_T, \sigma_T)$  for  $T_f^*$  instead of a single point estimate. This means that for every feature data point  $\mathbf{x}^*$ , the predicted  $T_f^*$  has normal distribution with mean value  $\mu_T$  and standard deviation  $\sigma_T$ .

The ML models for predicting the lattice parameters—the GP<sub>m</sub> and GP<sub>t</sub> models—take a single value of  $T_f^*$  instead of its probability distribution in the input space. Hence, for each synthetic composition ‘s’, we draw  $N$  random samples from its predicted distribution  $p(T_f^*|\mathbf{x}^*, \mathbf{x}, T_f)$  and combine them with the key physical features. For example, we draw  $N = 15000$  random sample from the  $p(T_f^*|\mathbf{x}^*, \mathbf{x}, T_f) \sim \mathcal{N}(\mu_T, \sigma_T)$  for  $T_f^*$ . These randomly drawn  $T_f^*$  samples are combined with the physical features as  $\{(T_i, eff_s, rcls, cs_s, rios)|i \in \{1, 2, \dots, N\}\}$  for a single synthetic composition ‘s’ for prediction of monoclinic lattice parameters by the GP<sub>m</sub> model. For each ‘i’, the GP<sub>m</sub> model predicts a normal distribution of monoclinic lattice parameters  $\mathcal{N}(\mu_i, \sigma_i)$ . Thus, we obtain  $N$  normal distributions of lattice parameters for 1 synthetic composition, which can be merged together into one normal distribution. We use the following expressions to evaluate the mean  $\mu^m$  and standard deviation  $\sigma^m$  of the merged distribution  $\mathcal{N}(\bar{\mu}_m, \bar{\sigma}_m)$  of monoclinic lattice parameters:

$$\bar{\mu}_m = \frac{1}{N} \sum_{i=1}^N \mu_i \quad (6)$$

$$\bar{\sigma}_m = \sqrt{\frac{1}{N} \sum_{i=1}^N (\mu_i^2 + \sigma_i^2) - \bar{\mu}_m^2} \quad (7)$$

Similarly, samples drawn from the distribution  $\mathcal{N}(\mu_T, \sigma_T^2)$  of  $T_f^*$  are also combined with  $\mathbf{x}^* = (eff, cs, en)$  to create the input space of the GP<sub>t</sub> model to predict the probability distribution of tetragonal lattice parameters for each synthetic composition. This approach of introducing probability distribution of  $T_f^*$  into the GP<sub>m</sub> and GP<sub>t</sub> model allows the propagation of the uncertainty associated with  $T_f^*$ —quantified by the 95% confidence interval  $(\mu_T - 1.96\sigma_T, \mu_T + 1.96\sigma_T)$  of the distribution  $\mathcal{N}(\mu_T, \sigma_T)$ —to the uncertainty associated with the distribution of the lattice parameters.

The predicted lattice parameters for all synthetic compositions allows for the calculation of cofactor conditions and identify compositions that closely satisfy the cofactor condition. The lattice parameters are used to calculate the average deformation tensor  $\mathbf{U}_f$ . For example, for the case of the twinned laminate that has a volume fraction  $(1 - f)$  of correspondence-1a and a volume fraction  $f$  of correspondence-2 ( $\mathbf{U}_i^{(1a)}/\mathbf{U}_j^{(2)}$ ), the average deformation stretch tensor is  $\mathbf{U}_f = \mathbf{U}_i^{(1a)} + f(\hat{\mathbf{a}} \otimes \mathbf{n})$ , which is used in the expression  $q(f) = \det(\mathbf{U}_f^T \mathbf{U}_f - \mathbf{I})$ . Similarly,  $\mathbf{U}_f = \mathbf{U}_i^{(1b)} + f(\hat{\mathbf{a}} \otimes \mathbf{n})$  for the case of twinned laminate having volume fraction  $(1 - f)$  from the correspondence-1b and volume fraction  $f$  from the correspondence-2. We calculate the  $\max|q(f)|$  value for the three cases where the twin structure has combination of correspondences from the set  $\mathbf{U} \in \{\mathbf{U}_i^{(1a)}/\mathbf{U}_j^{(2)}, \mathbf{U}_i^{(1b)}/\mathbf{U}_j^{(2)}, \mathbf{U}_i^{(2)}/\mathbf{U}_j^{(2)}\}$ .

For all synthetic compositions, we evaluate the middle eigenvalue  $\lambda_2^{(1a)}$ ,  $\lambda_2^{(1b)}$  and  $\lambda_2^{(2)}$  of the transformation stretch tensor of correspondences 1a, 1b and 2, and plot it with corresponding  $\max|q(f)|$  with  $\mathbf{U}_f = \mathbf{U}_i^{(1a)} + f(\hat{\mathbf{a}} \otimes \mathbf{n})$ ,  $\mathbf{U}_f = \mathbf{U}_i^{(1b)} + f(\hat{\mathbf{a}} \otimes \mathbf{n})$  and  $\mathbf{U}_f = \mathbf{U}_i^{(2)} + f(\hat{\mathbf{a}} \otimes \mathbf{n})$  respectively, as shown in Fig. 11(a). We find that there is strong correlation between  $\lambda_2$  and  $\max|q(f)|$  in all 3 cases. To check if the same trend is observed in the compositions fabricated for the XRD-experiments, we chose few compositions and plotted the  $\lambda_2$  vs.  $\max|q(f)|$  to observe a similar trend as shown in Fig. 11(b). The reason for the strong correlation is that most of the the maximum deviations calculated using the lattice parameters are obtained at the boundary point  $f = 0$  and  $f = 1$ . This simplifies the  $|q(f)|$  expression, for example, for twin structure with variants from correspondence-1a and -2 ( $\mathbf{U}_i^{(1a)}/\mathbf{U}_j^{(2)}$ ), if the maximum deviation exists at  $f = 0$ , this means  $q(f)$  simplifies to  $q(f) = \det[(\mathbf{U}_i^{(1a)})^T \mathbf{U}_i^{(1a)} - \mathbf{I}] = 0$ . Equivalently, in terms of the eigenvalues of correspondence-1a,  $q(f) = [(\lambda_1^{(1a)})^2 - 1][(\lambda_2^{(1a)})^2 - 1][(\lambda_3^{(1a)})^2 - 1] = 0$ . On the other hand, if the maximum deviation exist at the  $f = 1$  then  $q(f)$  simplifies to  $q(f) = \det[(\mathbf{U}_i^{(2)})^T \mathbf{U}_i^{(2)} - \mathbf{I}] = 0$  or, in terms of eigenvalues of the correspondence-2,  $q(f) = [(\lambda_1^{(2)})^2 - 1][(\lambda_2^{(2)})^2 - 1][(\lambda_3^{(2)})^2 - 1] = 0$ .

For the case of a twinned structure with variants  $\mathbf{U}_i^{(2)}/\mathbf{U}_j^{(2)}$  of correspondence 2, the twinned structure transforms into a pure phase having any variant  $\mathbf{U}_i^{(2)}$  of correspondence 2 at both  $f = 0$  and  $f = 1$ . Thus, for targeting specific synthetic composition to search for low hysteresis ceramic, we chose  $\lambda_2 = 1$  as the criteria instead of the  $\max|q(f)|$  criteria.

## 5.2 Selection of synthetic composition for experiment

Pang et. al. [25] proposed four design criteria to attain low hysteresis Zirconia based ceramic material, which are, (1) Middle eigenvalue of transformation stretch tensor  $\lambda_2 = 1$  of correspon-

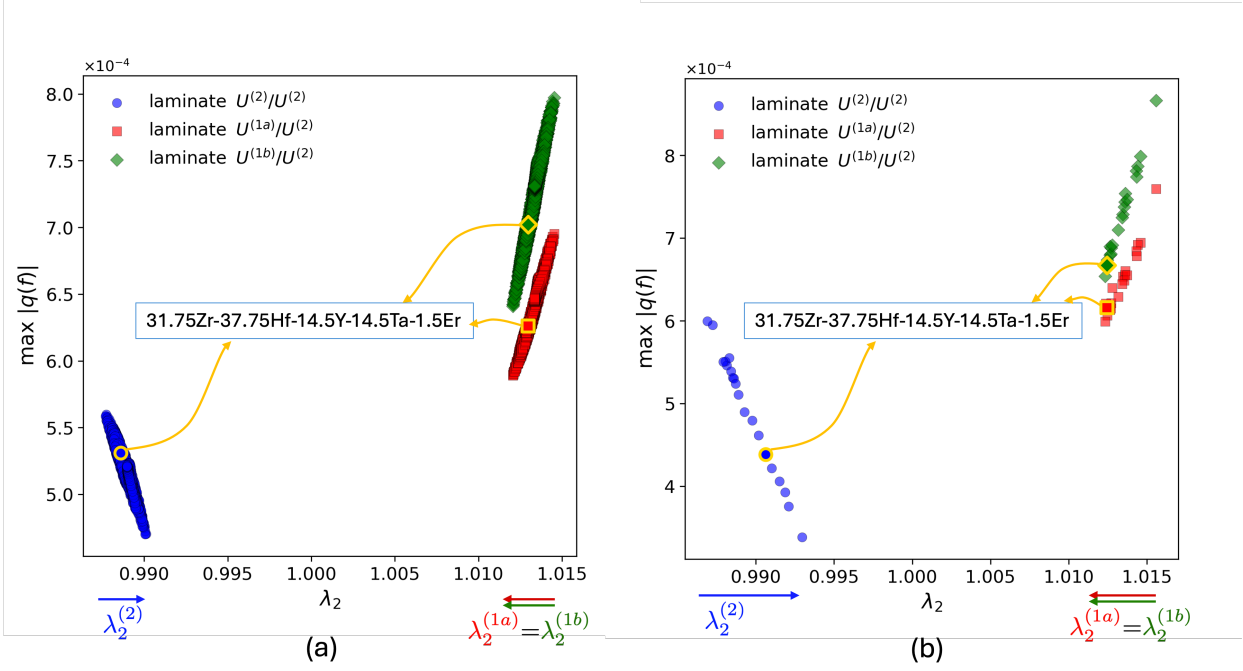


Figure 11: Correlation between  $\lambda_2^{(1a)}$ ,  $\lambda_2^{(1b)}$ ,  $\lambda_2^{(2)}$  and  $\max |q(f)|$  for lattice parameters of: (a) synthetic compositions predicted by the ML model (b) actual compositions measured by XRD-experiment. The highlighted data point in yellow color is selected based on predicted  $\lambda_2^{(2)}$  closest to 1 while satisfying the equidistant condition  $|\lambda_2^{(1a,1b)} - 1| = |\lambda_2^{(2)} - 1|$ .

dence 2, (2) Low transformation volume change ( $\Delta V/V$ ) (3) Solubility of dopants (4) High value of Martensite start temperature ( $M_s \geq 500^\circ C$ ). Using this design criteria, they discovered a low hysteresis Zirconia-based ceramic doped with 17Ti-3Al-6Cr with a hysteresis of 15 K. Hanlin et. al. [6] found the lowest hysteresis in the system  $(Zr_y Hf_{1-y} O_2)_{0.775} - (Y_{0.5} Nb_{0.5} O_2)_{0.225}$  at  $y = 0.45$  where an equidistant condition  $|\lambda_2^{(1a,1b)} - 1| = |\lambda_2^{(2)} - 1|$  is satisfied.

The predicted lattice parameters  $\bar{\mu}$  of the synthetic compositions are used to calculate the stretch tensor ' $\mathbf{U}$ ' of the three correspondences 1<sub>a</sub>, 1<sub>b</sub> and 2 and their middle eigenvalues  $\lambda_2^{(1a)}$ ,  $\lambda_2^{(1b)}$  and  $\lambda_2^{(2)}$  respectively. To search for low-hysteresis ceramic within synthetic compositions, the equidistant condition is closely satisfied along with design criteria proposed by Pang. Hence, the synthetic composition is selected that has the least value of  $|\lambda_2^{(1a,1b)} - 1| - |\lambda_2^{(2)} - 1|$ , along with (1)  $\lambda_2^{(2)} = 1$  (2) Low  $\Delta V/V$  (3) Solid solubility (4)  $M_s \geq 500^\circ C$ . We selected 31.75Zr-37.75Hf-14.5Y-14.5Ta-1.5Er among all synthetic compositions for experiments, since it closely satisfies the equidistant condition  $|\lambda_2^{(1a,1b)} - 1| - |\lambda_2^{(2)} - 1| = 0.0263$  along with the design criteria with predicted (1)  $\lambda_2^{(2)} = 0.9891$  (2)  $\Delta V/V = 3.27\%$  (3) all dopants are within solubility limits (4)  $T_f^* = 636.78^\circ C$ . This composition is also highlighted in Fig. 11 to show that the equidistant condition is not observed at the point where  $\lambda_2^{(2)}$  is closest to 1.

### 5.3 Experimental Methodology & results

The thermal measurements of transformation temperature and transformation enthalpy are performed by using a TA instruments SDT 650 machine capable of doing DTA measurements with a temperature range between room-temperature and 1500 °C. For samples that have one or more of the four temperatures used for thermal characterization below RT, a Netzsch DSC

204 F1 Phoenix with a minimum temperature of  $-160\text{ }^{\circ}\text{C}$  can be used. With the combined temperature range from  $-160\text{ }^{\circ}\text{C}$  to  $1500\text{ }^{\circ}\text{C}$  a throughout measurement of  $M_s$ ,  $M_f$ ,  $A_s$  and  $A_f$  for a large range of sample composition can be ensured.

For the determination of lattice parameters all samples underwent temperature controlled XRD investigations. The Rigaku SmartLab 9kW was employed for this task and all measurements were performed using mainly Cu  $K_{alpha}$  radiation. A Ni filter was used to reduce the intensity of Cu  $K_{beta}$  wavelength without the need for proper monochomatization. For temperature control the Anton Paar temperature stages DHS 1100 and DCS 350 were used. Those two stages combined allowed for precise XRD  $\theta/2\theta$  measurements in a temperature range between  $-100\text{ }^{\circ}\text{C}$  and  $1100\text{ }^{\circ}\text{C}$ . Having measured the transformation temperatures for the sample in question beforehand allows for very small temperature intervals during martensitic and austenitic transformations. These measurements moreover allowed to measure not only thermal expansion of individual lattice parameters of both, high and low temperature phase, but by performing Rietveld refinements on each measurement, the determination of relative phase fractions. Since the refinement is more robust with higher signal intensities, we opted to exclude data calculated from minority phases if the phase fraction dropped below 20%.

Those measurements are also used to ensure the absence of any secondary phases which can possibly be formed by limited solubility in the solid solution. The refinements were performed semi-automatically by using the batch processing capabilities of the software package TOPAS v6.

For the selected ceramic 31.75Zr-37.75Hf-14.5Y-14.5Ta-1.5Er, we have measured start and finish temperatures of Austenite  $A_s = 611^{\circ}\text{C}$ ,  $A_f = 661^{\circ}\text{C}$  and Martensite  $M_s = 518^{\circ}\text{C}$  and  $M_f = 480^{\circ}\text{C}$  and calculated the transformation temperature  $T_f^* = 0.5 * (M_s + A_f) = 589.5^{\circ}\text{C}$ . We also measured lattice parameters for this sample, as shown in Table 4. The ML predictions of lattice parameters for this composition are found to be in good agreement with experiments, as shown in Table 4. From the lattice parameters, we found the actual value of middle eigenvalue of correspondence-2 is  $\lambda_2 = 0.9921$ , and  $\Delta V/V = 3.65\%$ . The thermal hysteresis for this sample is  $\Delta T = 137^{\circ}\text{C}$ . Although this sample satisfies all design criteria, still it has a significantly high hysteresis.

To understand the role of dopant  $\text{Er}_2\text{O}_3$  in reducing the tetragonality ratio ( $c_t/a_t$ ), we calculate the  $(c_t/a_t) = 1.0258$  for 31.75Zr-37.75Hf-14.5Y-14.5Ta using predicted lattice parameters, and after addition of 1.5%  $\text{Er}_2\text{O}_3$  in this composition, the  $(c_t/a_t)$  ratio reduces to 1.0246, a 0.117% reduction in the tetragonality value. This implies that small amounts of  $\text{Er}_2\text{O}_3$  addition (up to solubility limits) in the Zr-Hf-Y-Ta ceramic system reduces its tetragonality ratio; however, it has a weak effect in reducing tetragonality.

Table 4: Comparison of predicted vs experimental values

	ML Predicted	Experimental	% Error
$T_f^*$	$638.76 \pm 65.97$	589.5	8.36 %
$a_m$	$5.1765 \pm 0.0021$	5.1778	0.025 %
$b_m$	$5.1967 \pm 0.0067$	5.1908	0.114 %
$c_m$	$5.3648 \pm 0.0070$	5.3667	0.035 %
$\beta$	$98.7273 \pm 0.0971$	98.7377	0.010 %
$a_t$	$3.6256 \pm 0.0075$	3.6255	0.003 %
$c_t$	$5.2539 \pm 0.0186$	5.2321	0.042 %

## 6 Conclusion

In summary, we have demonstrated a Gaussian process (GP) framework that can accurately predict the transformation temperature of a chosen ceramic system and its lattice parameters of both the monoclinic and tetragonal structure. The GP framework is used to predict lattice parameters of 5416 synthetic compositions. The lattice parameters are then used to evaluate the middle eigenvalue of the deformation stretch tensor  $\lambda_2$  and the  $\max|q(f)|$  value. We found a strong correlation between the  $\lambda_2$  and the  $\max|q(f)|$  value. This implies that the  $\lambda_2 = 1$  criteria is sufficient for the  $\text{ZrO}_2$ -based ceramic system doped with  $\text{HfO}_2$ ,  $\text{YTaO}_4$  and  $\text{Er}_2\text{O}_3$  to search for low hysteresis ceramics composition, as the maximum deviation values always decreases when  $\lambda_2$  approaches towards 1. We selected a synthetic composition 31.75Zr-37.75Hf-14.5Y-14.5Ta-1.5Er that closely satisfy the cofactor condition and fabricated it for a differential thermal analysis and X-ray diffraction experiments to measure its transformation temperature and lattice parameters respectively, which are found to be in good agreement with predicted values from the GP models. Also, with  $\lambda_2$  approaching towards 1, a single variant of martensite from any one correspondence becomes dominant instead of a twin structure with multiple correspondences from correspondences 1a, 1b and 2. Thus, the  $\lambda_2^{(1a)} = 1$ ,  $\lambda_2^{(1b)} = 1$  and  $\lambda_2^{(2)} = 1$  are the dominant compatibility conditions for this ceramic system with correspondences 1a, 1b and 2 in the martensite phase respectively.

The steps described in the GP framework could also be applied to new ceramic systems having additional dopants for accurate prediction of their transformation temperature and lattice parameters. Such machine learning models have applications in detecting synthetic compositions with predicted desired properties, thus reducing efforts in experiments by informing targeted values in the compositional space.

We selected a synthetic composition 31.75Zr-37.75Hf-14.5Y-14.5Ta-1.5Er that satisfied all four design criteria required to reduce the thermal hysteresis in  $\text{ZrO}_2$  based ceramics. However, in the differential thermal analysis experiment, we found a high value of thermal hysteresis:  $\Delta T = 137^\circ\text{C}$ . Thus, the current four criteria are not universal for ceramics, and they do not always result in low hysteresis ceramic. In the future work, there is a need to explore a new dopant that could reduce the tetragonality ratio of the parent phase to an extent that the ceramic system fully transforms from cubic to monoclinic. This is because the cubic to monoclinic phase transformation results in a greater number of variants of the martensite compared to the tetragonal to monoclinic transformation. This allows more variants to orient themselves to allow for large deformation during phase transformation and satisfy the cofactor conditions.

## References

- [1] Jun Cui, Yong S. Chu, Olugbenga O. Famodu, Yasubumi Furuya, Jae Hattrick-Simpers, Richard D. James, Alfred Ludwig, Sigurd Thienhaus, Manfred Wuttig, Zhiyong Zhang, and Ichiro Takeuchi. Combinatorial search of thermoelastic shape-memory alloys with extremely small hysteresis width. *Nature Materials*, 5(4):286–290, April 2006. Publisher: Nature Publishing Group.
- [2] Zhiyong Zhang, Richard D. James, and Stefan Müller. Energy barriers and hysteresis in martensitic phase transformations. *Acta Materialia*, 57(15):4332–4352, September 2009.
- [3] Robert Zarnetta, Ryota Takahashi, Marcus L. Young, Alan Savan, Yasubumi Furuya, Sigurd Thienhaus, Burkhard Maaß, Mustafa Rahim, Jan Frenzel, Hayo Brunken, Yong S. Chu, Vijay Srivastava, Richard D. James, Ichiro Takeuchi, Gunther Eggeler, and Alfred Ludwig. Identification of Quaternary Shape Memory Alloys with Near-Zero Thermal Hysteresis and Unprecedented Functional Stability. *Advanced Functional Materials*, 20(12):1917–1923, 2010. \_eprint: <https://onlinelibrary.wiley.com/doi/pdf/10.1002/adfm.200902336>.
- [4] R. D. James, Z. Zhang, R. D. James, and Z. Zhang. A Way to Search for Multiferroic Materials with “Unlikely” Combinations of Physical Properties. In Antoni Planes, Lluís Mañosa, and Avadh Saxena, editors, *Magnetism and Structure in Functional Materials*, pages 159–175. Springer Berlin Heidelberg, Berlin, Heidelberg, 2005.
- [5] Xian Chen, Vijay Srivastava, Vivekanand Dabade, and Richard D. James. Study of the cofactor conditions: Conditions of supercompatibility between phases. *Journal of the Mechanics and Physics of Solids*, 61(12):2566–2587, 2013.
- [6] Hanlin Gu, Jascha Rohmer, Justin Jetter, Andriy Lotnyk, Lorenz Kienle, Eckhard Quandt, and Richard D James. Exploding and weeping ceramics. *Nature*, 599(7885):416–420, 2021.
- [7] Kaushik Bhattacharya. *Microstructure of martensite : why it forms and how it gives rise to the shape-memory effect*. Oxford series on materials modelling ; 2. Oxford University Press, Oxford, 2003.
- [8] Li Jian and C. M. Wayman. Electron back scattering study of domain structure in monoclinic phase of a rare-earth orthoniobate LaNbO<sub>4</sub>. *Acta Metallurgica et Materialia*, 43(10):3893–3901, October 1995.
- [9] Li Jian and Richard D. James. Prediction of microstructure in monoclinic LaNbO<sub>4</sub> by energy minimization. *Acta Materialia*, 45(10):4271–4281, October 1997.
- [10] M. Pitteri and G. Zanzotto. Generic and non-generic cubic-to-monoclinic transitions and their twins<sup>1</sup>. *Acta Materialia*, 46(1):225–237, December 1998.
- [11] Hans Knüpfner, Robert V. Kohn, and Felix Otto. Nucleation Barriers for the Cubic-to-Tetragonal Phase Transformation. *Communications on Pure and Applied Mathematics*, 66(6):867–904, June 2013.
- [12] Christoph Chluba, Wenwei Ge, Rodrigo Lima de Miranda, Julian Strobel, Lorenz Kienle, Eckhard Quandt, and Manfred Wuttig. Shape memory alloys. Ultralow-fatigue shape memory alloy films. *Science (New York, N. Y.)*, 348(6238):1004–1007, May 2015.
- [13] Xiaoyue Ni, Julia R. Greer, Kaushik Bhattacharya, Richard D. James, and Xian Chen. Exceptional Resilience of Small-Scale Au<sub>30</sub>Cu<sub>25</sub>Zn<sub>45</sub> under Cyclic Stress-Induced Phase

- Transformation. *Nano Letters*, 16(12):7621–7625, December 2016. Publisher: American Chemical Society.
- [14] Robert V. Kohn and Stefan Müller. Branching of twins near an austenite—twinned-martensite interface. *Philosophical Magazine A*, 66(5):697–715, November 1992. Publisher: Taylor & Francis \_eprint: <https://doi.org/10.1080/01418619208201585>.
- [15] J. M. Ball and R. D. James. Fine phase mixtures as minimizers of energy. *Archive for Rational Mechanics and Analysis*, 100(1):13–52, March 1987.
- [16] Rémi Delville, Sakthivel Kasinathan, Zhiyong Zhang, Jan Van Humbeeck, Richard D. James, and Dominique Schryvers. Transmission electron microscopy study of phase compatibility in low hysteresis shape memory alloys. *Philosophical Magazine*, 90(1-4):177–195, January 2010.
- [17] J. K Mackenzie and J. S Bowles. The crystallography of martensite transformations II. *Acta Metallurgica*, 2:138–147, January 1954.
- [18] J. S Bowles and J. K Mackenzie. The crystallography of martensite transformations I. *Acta Metallurgica*, 2(1):129–137, January 1954.
- [19] Yintao Song, Xian Chen, Vivekanand Dabade, Thomas W. Shield, and Richard D. James. Enhanced reversibility and unusual microstructure of a phase-transforming material. *Nature*, 502(7469):85–88, October 2013. Publisher: Nature Publishing Group.
- [20] X. L. Meng, H. Li, W. Cai, S. J. Hao, and L. S. Cui. Thermal cycling stability mechanism of Ti<sub>50.5</sub>Ni<sub>33.5</sub>Cu<sub>11.5</sub>Pd<sub>4.5</sub> shape memory alloy with near-zero hysteresis. *Scripta Materialia*, 103:30–33, July 2015.
- [21] Maike Wegner, Hanlin Gu, Richard D. James, and Eckhard Quandt. Correlation between phase compatibility and efficient energy conversion in Zr-doped Barium Titanate. *Scientific Reports*, 10(1):3496, February 2020. Publisher: Nature Publishing Group.
- [22] Alan Lai, Zehui Du, Chee Lip Gan, and Christopher A. Schuh. Shape Memory and Superelastic Ceramics at Small Scales. *Science*, 341(6153):1505–1508, September 2013. Publisher: American Association for the Advancement of Science.
- [23] Patricia Pop-Ghe, Norbert Stock, and Eckhard Quandt. Suppression of abnormal grain growth in K<sub>0.5</sub>Na<sub>0.5</sub>NbO<sub>3</sub>: phase transitions and compatibility. *Scientific Reports*, 9(1):19775, December 2019. Publisher: Nature Publishing Group.
- [24] Y. G. Liang, S. Lee, H. S. Yu, H. R. Zhang, Y. J. Liang, P. Y. Zavalij, X. Chen, R. D. James, L. A. Bendersky, A. V. Davydov, X. H. Zhang, and I. Takeuchi. Tuning the hysteresis of a metal-insulator transition via lattice compatibility. *Nature Communications*, 11(1):3539, July 2020. Publisher: Nature Publishing Group.
- [25] Edward L. Pang, Gregory B. Olson, and Christopher A. Schuh. Low-hysteresis shape-memory ceramics designed by multimode modelling. *Nature*, 610:491–495, 10 2022.
- [26] Yudong Sui, Li’na Han, Yehua Jiang, and Quan Shan. Influence of Er<sub>2</sub>O<sub>3</sub> content on microstructure and mechanical properties of ZTA – TiO<sub>2</sub> composites. *Journal of Rare Earths*, 37:299–304, 3 2019.
- [27] H. C. Tong and C. M. Wayman. Characteristic temperatures and other properties of thermoelastic martensites. *Acta Metallurgica*, 22(7):887–896, July 1974.

- [28] Dae-Joon -J Kim. Effect of Ta<sub>2</sub>O<sub>5</sub>, Nb<sub>2</sub>O<sub>5</sub>, and HfO<sub>2</sub> alloying on the transformability of Y<sub>2</sub>O<sub>3</sub>-stabilized tetragonal HfO<sub>2</sub>. *Journal of the American Ceramic Society*, 73:115–120, 1990.
- [29] K. A. Khor and J. Yang. Lattice parameters, tetragonality (ca) and transformability of tetragonal zirconia phase in plasma-sprayed ZrO<sub>2</sub>-Er<sub>2</sub>O<sub>3</sub> coatings. *Materials Letters*, 31(1):23–27, 1997.
- [30] Mary Gurak, Quentin Flamant, Laetitia Laversenne, and David R. Clarke. On the yttrium tantalate – zirconia phase diagram. *Journal of the European Ceramic Society*, 38(9):3317–3324, 2018.
- [31] P. DURAN. The system erbia-zirconia. *Journal of the American Ceramic Society*, 60(11-12):510–513, 1977.
- [32] Mehrdad Zarinejad, Tim White, Yunxiang Tong, and Sajjad Rimaz. Martensitic transformation temperatures of ceramics. *Advanced Engineering Materials*, 12 2022.
- [33] J. Frenzel, A. Wiczorek, I. Opahle, B. Maaß, R. Drautz, and G. Eggeler. On the effect of alloy composition on martensite start temperatures and latent heats in Ni–Ti-based shape memory alloys. *Acta Materialia*, 90:213–231, May 2015.
- [34] Stephen Blyth. Karl pearson and the correlation curve, 1994.
- [35] E. Clementi, D. L. Raimondi, and W. P. Reinhardt. Atomic screening constants from scf functions. ii. atoms with 37 to 86 electrons. *The Journal of Chemical Physics*, 47:1300–1307, 1967.
- [36] D G Pettifor. Pheno enologigal and igrosgopig theories of structural stability, 1985.
- [37] A. L. Allred. Electronegativity values from thermochemical data. *Journal of Inorganic and Nuclear Chemistry*, 17(3):215–221, June 1961.
- [38] J. C. Slater. Atomic radii in crystals. *The Journal of Chemical Physics*, 41:3199–3204, 1964.
- [39] R. D. Shannon. Revised effective ionic radii and systematic studies of interatomic distances in halides and chalcogenides. *Acta Crystallographica Section A*, 32:751–767, 1976.
- [40] H. Hotop and W. C. Lineberger. Binding energies in atomic negative ions: Ii. *Journal of Physical and Chemical Reference Data*, 14:731–750, 1985.
- [41] Trevor Hastie, Robert Tibshirani, and Ryan Tibshirani. Best Subset, Forward Stepwise or Lasso? Analysis and Recommendations Based on Extensive Comparisons. *Statistical Science*, 35(4):579 – 592, 2020.
- [42] James Bergstra and Yoshua Bengio. Random search for hyper-parameter optimization. *J. Mach. Learn. Res.*, 13(null):281–305, feb 2012.
- [43] Sen Liu, Branden B Kappes, Behnam Amin-ahmadi, Othmane Benafan, Xiaoli Zhang, and Aaron P Stebner. Physics-informed machine learning for composition – process – property design: Shape memory alloy demonstration. *Applied Materials Today*, 22:100898, 2021.
- [44] Udesch M.H.U. Kankanamge, Johannes Reiner, Xingjun Ma, Santiago Corujeira Gallo, and Wei Xu. Machine learning guided alloy design of high-temperature NiTiHf shape memory alloys. *Journal of Materials Science*, 57:19447–19465, 2022.

- [45] Edgar C Bain and NY Dunkirk. The nature of martensite. *trans. AIME*, 70(1):25–47, 1924.
- [46] W.M. Lomer. The  $\beta \rightarrow \alpha$  transformation in uranium-1. 4 at. % chromium alloy. page 243, 1955.
- [47] K. Koumatos and A. Muehleman. Optimality of general lattice transformations with applications to the Bain strain in steel. *Proceedings of the Royal Society A: Mathematical, Physical and Engineering Sciences*, 472(2188):20150865, April 2016. Publisher: Royal Society.
- [48] Ashley N. Bucsek, Grant A. Hudish, Glen S. Bigelow, Ronald D. Noebe, and Aaron P. Stebner. Composition, Compatibility, and the Functional Performances of Ternary NiTiX High-Temperature Shape Memory Alloys. *Shape Memory and Superelasticity*, 2(1):62–79, March 2016.
- [49] Lei Zhang, Long-Qing Chen, and Qiang Du. Morphology of Critical Nuclei in Solid-State Phase Transformations. *Physical Review Letters*, 98(26):265703, June 2007. Publisher: American Physical Society.
- [50] J. C. Fisher, J. H. Hollomon, and D. Turnbull. Nucleation. *Journal of Applied Physics*, 19(8):775–784, August 1948.
- [51] M. S. Wechsler, D. S. Lieberman, and T. A. Read. On the theory of the formation of martensite. *Trans AIME*, 197:1503–1515, 1953.
- [52] Hanlin Gu, Lars Bumke, Christoph Chluba, Eckhard Quandt, and Richard D. James. Phase engineering and supercompatibility of shape memory alloys. *Materials Today*, 21(3):265–277, April 2018.
- [53] Patrick M. Kelly and L.R. Francis Rose. The martensitic transformation in ceramics — its role in transformation toughening. *Progress in Materials Science*, 47(5):463–557, 2002.
- [54] M. Hayakawa, N. Kuntani, and M. Oka. Structural study on the tetragonal to monoclinic transformation in arc-melted zro2-2mol.%y2o3—i. experimental observations. *Acta Metallurgica*, 37(8):2223 – 2228, 1989.
- [55] M. Hayakawa and M. Oka. Structural study on the tetragonal to monoclinic transformation in arc-melted zro2-2mol.%y2o3—ii. quantitative analysis. *Acta Metallurgica*, 37(8):2229 – 2235, 1989.
- [56] Edward L. Pang, Caitlin A. McCandler, and Christopher A. Schuh. Reduced cracking in polycrystalline zro2-ceo2 shape-memory ceramics by meeting the cofactor conditions. *Acta Materialia*, 177:230 – 239, 2019.